Petroleum Science 19 (2022) 2810–2829

Contents lists available at ScienceDirect

Petroleum Science

journal homepage: www.keaipublishing.com/en/journals/petroleum-science

Original Paper

A new model for predicting hydraulic fracture penetration or termination at an orthogonal interface between dissimilar formations

Yu Zhao [a, b], Yong-Fa Zhang [a, b, c, *], Guo-Dong Tian [c], Chao-Lin Wang [a, b], Jing Bi [a, b]

[a] College of Civil Engineering, Guizhou University, Guiyang, 550025, Guizhou, China
[b] Guizhou Provincial Key Laboratory of Rock and Soil Mechanics and Engineering Safety (Guizhou University), Guiyang, 550025, Guizhou, China
[c] School of Civil Engineering, Chongqing University, Chongqing, 400045, China

ARTICLE INFO

Article history:
Received 21 February 2022
Received in revised form
4 August 2022
Accepted 5 August 2022
Available online 10 August 2022

Edited by Yan-Hua Sun

Keywords:
Analytical model
Hydraulic fracture
Interface of dissimilar materials
Vertical propagation behavior
Parametric sensitivity analysis

ABSTRACT

Vertical height growth of hydraulic fractures (HFs) can unexpectedly penetrate a stratigraphic interface and propagate into neighboring layers, thereby resulting in low gas-production efficiency and high risk of groundwater contamination or fault reactivation. Understanding of hydraulic fracture behavior at the interface is of pivotal importance for the successful development of layered reservoirs. In this paper, a two-dimensional analytical model was developed to examine HF penetration and termination behavior at an orthogonal interface between two dissimilar materials. This model involves changes in the stress singularity ahead of the HF tip, which may alter at the formation interface due to material heterogeneity. Three critical stress conditions were considered to assess possible fracture behavior (i.e., crossing, slippage, and opening) at the interface. Then, this model was verified by comparing its theoretical predictions to numerical simulations and three independent experiments. Good agreement with the simulation results and experimental data was observed, which shows the validity and reliability of this model. Finally, a parametric study was conducted to investigate the effects of key formation parameters (elastic modulus, Poisson's ratio, and fracture toughness) between adjacent layers. These results indicate that the variation in the introduced parameters can limit or promote vertical HF growth by redistributing the induced normal and shear stresses at the interface. Among the three studied parameters, Poisson's ratio has the least influence on the formation interface. When the fracture toughness and elastic modulus of the bounding layer are larger than those of the pay zone layer, the influence of fracture toughness will dominate the HF behavior at the interface; otherwise, the HF behavior will more likely be influenced by elastic modulus.

1. Introduction

Unconventional hydrocarbon reservoirs, such as tight sandstones and shales, are characterized by ultralow permeability and porosity (Zhao et al., 2018, 2020). To effectively develop these reservoirs, inducing fractures by fluid injection, known as hydraulic fracturing, has become an essential technique for enhancing reservoir permeability and stimulating gas production. Hydraulic fractures (hereafter called HF) are created after massive high-pressure fluid is injected into the formation rocks. Owing to the difference in stress conditions, rock properties, fracturing fluid properties, and interfacial strength between adjacent strata (Guo et al., 2017; Tang et al., 2019; Zhao et al., 2021a), the HF propagation will inevitably be disturbed and complicated on a wide variety of length scales. As an HF progressively approaches a stratigraphic interface, the stress induced by the HF-tip singularity will project a considerable stress component at the interface, which may cause the interface to deform and fail (Lu et al., 2015; van Eekelen, 1982; Wang et al., 2015; Zhao et al., 2021b). The deformation and failure of the interface results in unexpected vertical fractures penetrating the interface and growing into neighboring strata, thereby reducing the exploitation efficiency and increasing the risk of water contamination and fault reactivation (Jabbari et al., 2017; Rodriguez et al., 2020; Zhang et al., 2020a). For better HF height containment, it is necessary to understand the stress field and stability of the formation interfaces in the vicinity of a propagating HF.

Prediction and containment of HF height growth is a critical issue in designing safe and economical hydraulic fracturing practices (Gao and Ghassemi, 2020; Weng et al., 2018; Zhang and Jeffrey, 2008). The initial HF propagation follows the least resistance principle and moves along its mechanically preferential propagation path (Tan et al., 2017; Yin et al., 2020). In the presence

* Corresponding author. College of Civil Engineering, Guizhou University, Guiyang, 550025, Guizhou, China.
E-mail address: zyfcqu@126.com (Y.-F. Zhang).

https://doi.org/10.1016/j.petsci.2022.08.002

List of symbols

C	Cohesion of the interface
E_1	Elastic modulus of the bounding layer at the HF (Formation 1)
E_2	Elastic modulus of the pay zone layer at the HF (Formation 2)
f	Friction coefficient of the interface
HF	Hydraulic fracture
K_1	Opening (Mode I) stress intensity factor of HF tip
K_2	Shearing (Mode II) stress intensity factor of HF tip
K_{IC1}	Fracture toughness of the bounding layer of the HF (Formation 1)
P_{HF}	Fluid pressure inside the HF
r_c	Critical radius of the nonlinear zone ahead of the HF tip
T_0	Tensile strength of the rock in front of the HF tip
u_{ri}	Radial displacement in the ith zone
μ_j	Shear modulus of the rock in the jth zone ($j = 1, 2, 3$)
ν_1	Poisson's ratio of the bounding layer at the HF (Formation 1)
ν_2	Poisson's ratio of pay zone layer at the HF (Formation 2)
$\nu_{\theta i}$	Circumferential displacement in the ith zone
$x_{critical}$	Horizontal distance away from the HF tip on the x-axis
λ	Dimensionless eigenvalue of the interface
σ_1	Maximum principal stress at the critical position ($x_{critical}$)
σ_h	Horizontal *in-situ* stress
σ_N	Total normal stress acting on the interface
σ_r	Radial stress component
σ_v	Vertical *in-situ* stress
σ_θ	Circumferential stress component near the interface
τ	Total shear stress acting on the interface
$\tau_{r\theta}$	Shear stress component on the interface induced by HF tip singularity

of a stratigraphic interface between different rock materials, the HF can penetrate the interface or be terminated by dilation and slippage at the interface, which has been previously demonstrated by field observations (Fisher and Warpinski, 2012; Warpinski, 2011) and laboratory experiments (Cheng et al., 2015; Zou et al., 2017).

To clarify the vertical propagation mechanism of the HF, many scholars have undertaken numerous experiment and simulation works on how a stratigraphic interface affects the vertical HF propagation behavior (Simonson et al., 1978; Warpinski et al., 1982; Zhao et al., 2022a; Zhang et al., 2017a). Through analyzing the stress intensity factor at the crack tip, Simonson et al. (1978) discussed the effect of material properties, *in-situ* stress and hydrostatic pressure gradients on vertical HF growth and found that an HF could easily break into the bounding layers provided that the stiffness of the pay zone was higher than that of the adjacent bounding layers. Otherwise, the HF was contained inside the pay zone. Warpinski et al. (1982) conducted mine-back experiments to explore the dominant factors that controlled the growth of HF height. The results revealed that the heterogeneity in elastic properties between the reservoir rock and the bounding formation had little effect on the large-scale HF propagation. On the other hand, the steep gradients and discontinuities in the magnitude of the minimum *in-situ* stress acted as barriers for HF growth. This phenomenon has been confirmed through both numerical modeling and laboratory experiments (Fung et al., 1987; Tan et al., 2019; Zhang et al., 2019). Therefore, the *in-situ* stress contrast between adjoining layers is recognized as the dominant factor affecting fracture height growth in most hydraulic fracturing scenarios.

Moreover, the elastic modulus contrast between the reservoir rock and the barrier layer has also been identified with great importance in influencing HF height containment when encountering a stratigraphic interface (Cook and Erdogan, 1972). Gu and Siebrits (2008) demonstrated that high modulus in the reservoir layer (pay zone) was adverse to HF height containment, particularly when the horizontal *in-situ* stress differences were much greater than the net fluid pressure. This result could be attributable to the relation between the net fluid pressure and the layer's elastic modulus: the higher elastic modulus of a layer generates a more significant net fluid pressure within the HF, which promotes HF propagation in the vertical direction (Smith et al., 2001). After analyzing the real-time HF growth based on fracture-mapping technology, Fisher and Warpinski (2012) reported that high modulus contrasts restricted fluid flow and had a pronounced effect on the increase of fracture width. Zhuang et al. (2020) simulated HF height propagation in naturally-layered media using the phase-field method, which indicated that the HF penetrated or deflected in a soft-to-stiff formation configuration, while only penetration was observed in a stiff-to-soft formation configuration. In this regard, the effect of the elastic modulus on the HF height growth becomes somewhat complex. The restrictive effect of low-modulus layers surrounding a higher-modulus pay zone on the HF height can be radically attributed to the lower stress-intensity factor at the interface. However, Xing et al. (2018) experimentally confirmed that relatively large fracture toughness of the bounding layer can also achieve the same outcome. In line with Thiercelin et al. (1989) and Gu and Siebrits (2008), a significant fracture toughness contrast in adjacent layers induced a high pressure and restricted HF height growth. Therefore, it is necessary to separately consider the effects of fracture toughness and elastic modulus on HF growth to obtain a fundamental understanding of HF behavior at stratigraphic interfaces. In addition to the elastic modulus and fracture toughness, Poisson's ratio also influences the vertical propagation of the HF height. Through field monitoring, Labudovic (1984) found that HFs could easily cross an interface when the Poisson's ratio of the bounding layer was lower than that of the pay zone. However, reliable predictions of HF propagation and containment behavior in layered formations are still scarce, and whether the HF height is contained by interface slippage or opening is also unclear, which merits further investigation.

In general, previous efforts have attempted to elucidate how the HF propagates when encountering an interface in layered formations. Although the *in-situ* stress has been ranked as a crucial parameter dominating fracture height growth in previous works, these studies have yet to reach a consensus on the influence of different material properties (elastic modulus, Poisson's ratio, and fracture toughness) on the HF behavior at the interface. Furthermore, current works are increasingly considering as many factors as possible (fluid viscosity, environmental temperature, flow rate, etc.), but few studies have concentrated on the variation in the stress singularity at the HF tip. According to Warpinski et al. (1982) and Yue et al. (2020), the nature ($-1/2$) of HF-tip stress singularities in a homogenous medium will change as the HF reaches the interface, which may play a crucial role in the subsequent disruption of the HF behavior. Therefore, predicting vertical HF

propagation behavior at a stratigraphic interface remains an open research topic, implying that new insights should be provided to conduct further research.

In this study, a new interface model of a composite rock mass considering changes in the stress singularity at the HF tip is developed to predict subsequent HF behavior (termination or penetration) at the interface. This model is validated by comparing the results of the presented model to numerical simulations and previously published experimental observations. In addition, through parametric sensitivity analysis, the effects of the elastic modulus, Poisson's ratio, and fracture toughness are separately discussed, which further verifies the reliability of the presented model.

2. Problem formulation

2.1. Interface model of composite rock mass

As Fig. 1 shows, a plane strain interface model of a linear elastic composite rock mass is constructed with an HF (blue semi ellipse) orthogonally encountering an unbounded frictional interface (red line). The so-called unbounded frictional interface refers to an interface with infinite length and obeys a linear friction law (or more precisely Mohr-Coulomb criterion) in line with Renshaw and Pollard (1995). The vertical direction corresponds to the major growth orientation of HFs, as is currently observed in actual hydraulic fracturing processes (Flewelling et al., 2013; Zhang et al., 2017b). The initial stress field is dominated by far-field *in-situ* stress components σ_v and σ_h, parallel and perpendicular to the HF in the *Oxy* coordinate system, respectively. For convenience, a polar coordinate system is additionally established with the HF tip as the origin *O* and the *y*-axis as the polar axis. Formation 1 and Formation 2 correspond to two different types of strata. Specifically, Formation 1 is the bounding layer that denotes the target formation of the propagating HF, and Formation 2 represents the pay-zone layer that initially contains the propagating HF. To evaluate the stress field around the HF tip, this model is divided into three zones (Zone 1, Zone 2, and Zone 3 as shown in Fig. 1) by the stratigraphic interface and the HF. The stratigraphic interface between Formation 1 and Formation 2 is assumed to be a thin and firm interlayer with friction and cohesion. The model is assumed to be stable until the HF reaches the interface (the approaching process is neglected).

2.2. Analytical solution of the stress on the stratigraphic interface

According to interface fracture mechanics (Keller et al., 2010), complex variable functions are often adopted to calculate the stress field ahead of the HF tip when a crack extends towards a stratigraphic interface. In polar coordinates, the stress can be expressed by Goursat's formula as (Greengard et al., 1996)

$$\begin{aligned}\sigma_\theta + \mathrm{i}\tau_{r\theta} &= \varphi' + \overline{\varphi'} + \mathrm{e}^{2\mathrm{i}\theta}[\bar{z}\varphi'' + \psi'] \\ \sigma_r - \mathrm{i}\tau_{r\theta} &= \varphi' + \overline{\varphi'} - \mathrm{e}^{2\mathrm{i}\theta}[\bar{z}\varphi'' + \psi']\end{aligned} \tag{1}$$

where φ and ψ are Goursat functions; θ is the polar angle relative to the positive *y*-axis; σ_r represents the radial stress component; σ_θ is the circumferential stress component; and $\tau_{r\theta}$ denotes the shear stress component, as shown in Fig. 1.

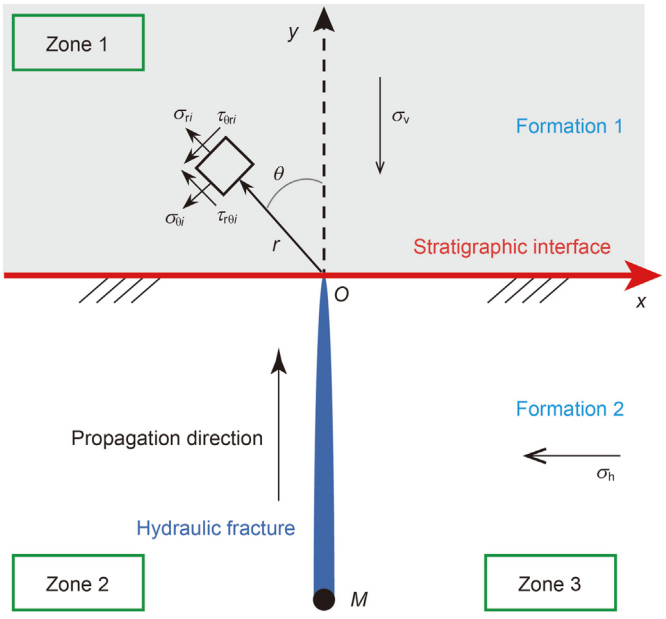

Fig. 1. Schematic diagram of interface model of the composite rock mass.

Here, we assume the Goursat's stress functions of the different zones in Fig. 1 to be

$$\varphi_j = A_j z^\lambda + B_j z^{\bar{\lambda}}, \quad \psi_j = C_j z^\lambda + D_j z^{\bar{\lambda}}, \quad j = 1,\ 2,\ 3 \tag{2}$$

where λ is the interface eigenvalue, which is essentially an undetermined coefficient relevant to the interface geometry and the mechanical properties of the formation medium. This parameter also represents the principal stress (or displacement) distribution characteristics (Keller et al., 2010). *z* is a complex number related to spatial positions; A_j, B_j, C_j and D_j are undetermined coefficients, and the subscript $j = 1, 2, 3$ correspond to Zone 1, Zone 2 and Zone 3, respectively.

Taking $z = r\mathrm{e}^{\mathrm{i}\theta}$ ($\mathrm{i} = \sqrt{-1}$) and combining Eqs. (1) and (2), we obtain the stress field of different zones:

$$\begin{cases} \sigma_{\theta j} + \mathrm{i}\tau_{r\theta j} = r^{\lambda-1}\left[A_j\lambda^2\mathrm{e}^{\mathrm{i}(\lambda-1)\theta} + \overline{B_j}\lambda\mathrm{e}^{-\mathrm{i}(\lambda-1)\theta} + C_j\lambda\mathrm{e}^{\mathrm{i}(\lambda+1)\theta}\right] \\ \qquad\qquad + r^{\bar{\lambda}-1}\left[B_j\bar{\lambda}^2\mathrm{e}^{\mathrm{i}(\bar{\lambda}-1)\theta} + \overline{A_j}\bar{\lambda}\mathrm{e}^{-\mathrm{i}(\bar{\lambda}-1)\theta} + D_j\bar{\lambda}\mathrm{e}^{\mathrm{i}(\bar{\lambda}+1)\theta}\right] \\ 2\mu_j(\sigma_{\theta j} + \mathrm{i}\tau_{r\theta j}) = r^{\lambda}\left[A_j\kappa_j\mathrm{e}^{\mathrm{i}(\lambda-1)\theta} - \overline{B_j}\lambda\mathrm{e}^{-\mathrm{i}(\lambda-1)\theta} - \overline{D_j}\mathrm{e}^{-\mathrm{i}(\lambda+1)\theta}\right] \\ \qquad\qquad + r^{\bar{\lambda}}\left[B_j\kappa_j\mathrm{e}^{\mathrm{i}(\bar{\lambda}-1)\theta} - \overline{A_j}\bar{\lambda}\mathrm{e}^{-\mathrm{i}(\bar{\lambda}-1)\theta} - \overline{C_j}\mathrm{e}^{-\mathrm{i}(\bar{\lambda}+1)\theta}\right] \end{cases} \tag{3}$$

where μ_j is the rock's shear modulus in the *j*th zone and can be expressed by the corresponding elastic modulus (E_j) and Poisson's ratio (ν_j) via $\mu_j = \frac{E_j}{2(1+\nu_j)}$, $j = 1,\ 2,\ 3$; and κ_j equals $3 - 4\nu_j$ for the plane strain problems according to Dundurs (1967).

According to Ham and Kwon (2020), λ is real. Therefore, Eq. (3) can alternatively be presented as

$$\begin{cases} \sigma_{\theta j} + \mathrm{i}\tau_{r\theta j} = r^{\lambda-1}\left[(A_j + B_j)\lambda^2\mathrm{e}^{\mathrm{i}(\lambda-1)\theta} + (\overline{A_j} + \overline{B_j})\lambda\mathrm{e}^{-\mathrm{i}(\lambda-1)\theta} + (C_j + D_j)\lambda\mathrm{e}^{\mathrm{i}(\lambda+1)\theta}\right] \\ 2\mu_j(\sigma_{\theta j} + \mathrm{i}\tau_{r\theta j}) = r^{\lambda}\left[(A_j + B_j)\kappa_j\mathrm{e}^{\mathrm{i}(\lambda-1)\theta} - (\overline{A_j} + \overline{B_j})\lambda\mathrm{e}^{-\mathrm{i}(\lambda-1)\theta} - (\overline{C_j} + \overline{D_j})\mathrm{e}^{-\mathrm{i}(\lambda+1)\theta}\right] \end{cases} \tag{4}$$

Regarding the composite rock mass, the mechanical continuity condition of the stratigraphic interface between two isotropic and elastic formations should be

$$(x<0)\begin{cases} u_{r1}\left(r,\frac{\pi}{2}\right)=u_{r2}\left(r,\frac{\pi}{2}\right),\ \ v_{\theta1}\left(r,\frac{\pi}{2}\right)=v_{\theta2}\left(r,\frac{\pi}{2}\right) \\ \sigma_{\theta1}\left(r,\frac{\pi}{2}\right)=\sigma_{\theta2}\left(r,\frac{\pi}{2}\right),\ \ \tau_{r\theta1}\left(r,\frac{\pi}{2}\right)=\tau_{r\theta2}\left(r,\frac{\pi}{2}\right) \end{cases}$$
$$(x>0)\begin{cases} u_{r1}\left(r,-\frac{\pi}{2}\right)=u_{r3}\left(r,-\frac{\pi}{2}\right),\ \ v_{\theta1}\left(r,-\frac{\pi}{2}\right)=v_{\theta3}\left(r,-\frac{\pi}{2}\right) \\ \sigma_{\theta1}\left(r,-\frac{\pi}{2}\right)=\sigma_{\theta3}\left(r,-\frac{\pi}{2}\right),\ \ \tau_{r\theta1}\left(r,-\frac{\pi}{2}\right)=\tau_{r\theta3}\left(r,-\frac{\pi}{2}\right) \end{cases} \tag{5}$$

where $\pm\frac{\pi}{2}$ corresponds to the polar angle θ; u_{rj} represents the radial displacement in the jth zone; and $v_{\theta j}$ represents the circumferential displacement in the jth zone.

The stress boundary conditions on the HF are

$$\begin{cases} \sigma_{\theta2}(r,\pi)=0,\ \ \tau_{r\theta2}(r,\pi)=0 \\ \sigma_{\theta3}(r,-\pi)=0,\ \ \tau_{r\theta3}(r,-\pi)=0 \end{cases} \tag{6}$$

Note that the energy consumption associated with viscous drags of fluid flow within the HF is neglected during the HF propagation process, and a uniformly pressurized HF with null (fluid) pressure gradient (Adachi, 2001) is focused on. In addition, according to Renshaw and Pollard (1995) and Detournay (2004), a fluid lag is expected behind the HF tip and usually remains exponentially small for a large dimensionless toughness. Thus, the fluid lag is assumed to be insignificant under current hydraulic fracturing conditions.

Substituting Eq. (4) into Eqs. (5) and (6), we can obtain

$$\begin{cases} A_1\lambda+\overline{B_1}\mathrm{e}^{-\mathrm{i}(\lambda-1)\pi}+C_1\mathrm{e}^{i\pi}=A_2\lambda+\overline{B_2}\mathrm{e}^{-\mathrm{i}(\lambda-1)\pi}+C_2\mathrm{e}^{i\pi} \\ B_1\lambda+\overline{A_1}\mathrm{e}^{-\mathrm{i}(\lambda-1)\pi}+D_1\mathrm{e}^{i\pi}=B_2\lambda+\overline{A_2}\mathrm{e}^{-\mathrm{i}(\lambda-1)\pi}+D_2\mathrm{e}^{i\pi} \end{cases} \tag{6a}$$

$$\begin{cases} \Gamma\left[A_1\kappa_1-\overline{B_1}\lambda\mathrm{e}^{-\mathrm{i}(\lambda-1)\pi}-\overline{D_1}\mathrm{e}^{-\mathrm{i}\lambda\pi}\right]=A_2\kappa_2-\overline{B_2}\lambda\mathrm{e}^{-\mathrm{i}(\lambda-1)\pi}-\overline{D_2}\mathrm{e}^{-\mathrm{i}\lambda\pi} \\ \Gamma\left[B_1\kappa_1-\overline{A_1}\lambda\mathrm{e}^{-\mathrm{i}(\lambda-1)\pi}-\overline{C_1}\mathrm{e}^{-\mathrm{i}\lambda\pi}\right]=B_2\kappa_2-\overline{A_2}\lambda\mathrm{e}^{-\mathrm{i}(\lambda-1)\pi}-\overline{C_2}\mathrm{e}^{-\mathrm{i}\lambda\pi} \end{cases} \tag{6b}$$

$$\begin{cases} A_1\lambda+\overline{B_1}\mathrm{e}^{\mathrm{i}(\lambda-1)\pi}+C_1\mathrm{e}^{-i\pi}=A_3\lambda+\overline{B_3}\mathrm{e}^{\mathrm{i}(\lambda-1)\pi}+C_3\mathrm{e}^{-i\pi} \\ B_1\lambda+\overline{A_1}\mathrm{e}^{\mathrm{i}(\lambda-1)\pi}+D_1\mathrm{e}^{-i\pi}=B_3\lambda+\overline{A_3}\mathrm{e}^{\mathrm{i}(\lambda-1)\pi}+D_3\mathrm{e}^{-i\pi} \end{cases} \tag{6c}$$

$$\begin{cases} \Gamma\left[A_1\kappa_1-\overline{B_1}\lambda\mathrm{e}^{\mathrm{i}(\lambda-1)\pi}-\overline{D_1}\mathrm{e}^{\mathrm{i}\lambda\pi}\right]=A_3\kappa_2-\overline{B_3}\lambda\mathrm{e}^{\mathrm{i}(\lambda-1)\pi}-\overline{D_3}\mathrm{e}^{\mathrm{i}\lambda\pi} \\ \Gamma\left[B_1\kappa_1-\overline{A_1}\lambda\mathrm{e}^{\mathrm{i}(\lambda-1)\pi}-\overline{C_1}\mathrm{e}^{\mathrm{i}\lambda\pi}\right]=B_3\kappa_2-\overline{A_3}\lambda\mathrm{e}^{\mathrm{i}(\lambda-1)\pi}-\overline{C_3}\mathrm{e}^{\mathrm{i}\lambda\pi} \end{cases} \tag{6d}$$

$$\begin{cases} A_2\lambda+\overline{B_2}\mathrm{e}^{-2\mathrm{i}\lambda\pi}+C_2=0 \\ B_2\lambda+\overline{A_2}\mathrm{e}^{-2\mathrm{i}\lambda\pi}+D_2=0 \end{cases} \tag{6e}$$

$$\begin{cases} A_3\lambda+\overline{B_3}\mathrm{e}^{2\mathrm{i}\lambda\pi}+C_3=0 \\ B_3\lambda+\overline{A_3}\mathrm{e}^{2\mathrm{i}\lambda\pi}+D_3=0 \end{cases} \tag{6f}$$

where $\kappa_i=3-4\nu_i$ (ν_i is the Poisson's ratio of Formation i, $i=1,2$) for the plane strain problem.

Combining Eqs. (6a)-(6f), after a series of parameter replacements and simplifications, as shown in Appendix A, a reduced formula of λ is finally obtained:

$$\frac{\alpha+\beta^2+\left(1-\beta^2\right)\cos\lambda\pi}{2\lambda^2}=(1-\beta)(\alpha-\beta) \tag{7}$$

where α and β are Dundurs' parameters named after Dundurs (1967) and subsequently redefined by Bogy (1968) as

$$\begin{cases} \alpha=\dfrac{(\kappa_2+1)-\Gamma(\kappa_1+1)}{(\kappa_2+1)+\Gamma(\kappa_1+1)}=\dfrac{\mu_1(\kappa_2+1)-\mu_2(\kappa_1+1)}{\mu_1(\kappa_2+1)+\mu_2(\kappa_1+1)} \\ \beta=\dfrac{(\kappa_2-1)-\Gamma(\kappa_1-1)}{(\kappa_2+1)+\Gamma(\kappa_1+1)}=\dfrac{\mu_1(\kappa_2-1)-\mu_2(\kappa_1-1)}{\mu_1(\kappa_2+1)+\mu_2(\kappa_1+1)} \end{cases} \tag{8}$$

Note that μ_1 and μ_2 correspond to the shear modulus of Formation 1 and Formation 2, respectively.

Similarly, after some form transformations of Eqs. (6a)-(6f), as detailed in Appendix B, the induced stress components applied on the stratigraphic interface can be derived

$$\sigma_{\theta1}+\mathrm{i}\tau_{r\theta1}=\frac{r^{\lambda-1}\mathrm{e}^{\frac{\mathrm{i}(\lambda-1)\pi}{2}}}{(\lambda+b)^2-(1+c)(1+\overline{c})} \begin{Bmatrix} K\left[\lambda^2-b^2+(1+\overline{c})\mathrm{e}^{-\mathrm{i}\lambda\pi}+c(1+\overline{c})\right] \\ +\overline{K}\left[-(\lambda+b)\mathrm{e}^{-\mathrm{i}\lambda\pi}-\lambda(1+2c)+b\right] \end{Bmatrix} \tag{9}$$

where K is the stress intensity factor of the HF tip; b and c are the dimensionless intermediate parameters, and their expressions (i.e., Eqs. (B.11), (B.7), and (B.8)) can be found in Appendix B.

If the elastic modulus E_i and Poisson's ratio ν_i of the bounding and pay zone layers are given, α and β can be determined by Eq. (8). Then, combining Eq. (7), the interface eigenvalue λ can be obtained. After substituting λ into Eqs. (B.7) and (B.8) and taking the stress intensity factor as mode I fracture toughness (critical stress intensity factor), the stress component on the interface (Eq. (9)) can be derived. Considering the effect of the remote *in-situ* stress field, we can further obtain the total normal and shear stresses on the stratigraphic interface:

$$\sigma_{\mathrm{N}}=\sigma_{\theta1}+\sigma_{\mathrm{v}},\ \ \tau=\tau_{r\theta1} \tag{10}$$

where σ_{N} is the total normal stress (that acts along the y-direction); and τ is the shear stress resolved on the interface (that acts along the x-direction).

2.3. Critical stress conditions for HF behavior

The singular stress field near the HF tip is also quantitatively investigated (Warpinski et al., 1982). A quantitative parameter, stress intensity factor, is adopted to characterize the singularity at the stress field and predict the HF behavior upon encountering the stratigraphic interface. However, in the composite rock mass, the stress intensity factor at the HF tip should reflect the influence of the differential mechanical properties of the two formations on both sides of the interface. Moreover, as an HF contacts the interface at an arbitrary angle (nonorthogonal angle), the stress ahead of the fracture tip will exhibit an apparent oscillating singularity on the interface, which significantly differs from the stress intensity factor in a homogeneous medium.

With known α and β values in Eq. (8), the interface eigenvalue λ can be derived from Eq. (7). When the HF orthogonally intersects the stratigraphic interface, the interface eigenvalue λ will be a real solution rather than a complex number due to the geometric symmetry of this special case, indicating that the stress field may not exhibit an oscillating singularity. Therefore, the induced stress field (Eq. (B.9)) becomes

$$(\sigma_{\theta 1} + \mathrm{i}\tau_{r\theta 1})_{\theta=0} = r^{\lambda-1}K = r^{\lambda-1}(K_1 + \mathrm{i}K_2) \tag{11}$$

where $\lambda-1$ represents the stress singularity.

In the case of $\lambda = 1/2$, the opening (K_1) and shearing (K_2) modes of stress intensity factors have the same dimensions as homogeneous materials. However, for $\lambda \neq 1/2$, K_1 and K_2 in the composite rock mass possess different dimensions. In addition, the magnitudes of K_1 and K_2 are correlated with the normal and shear stresses near the HF tip. Given the orthogonal orientation between the HF and the interface, the shearing mode of the stress intensity factor is ignored, i.e., $K_2 = 0$ and $K_1 = K_{IC}$.

To ensure the validity of linear elastic fracture mechanics (LEFM), a critical radius (r_c) of the nonlinear zone ahead of the HF tip was introduced in accordance with Renshaw and Pollard (1995), who assumed that r_c delineated the scope of the nonlinear (plastic) zone produced by the singularity at the HF tip so that the rock outside the nonlinear region was considered to follow LEFM.

For an orthogonal intersection case (Fig. 1), the stress field near a fracture tip is approximated as (Gu et al., 2012)

$$\begin{cases} \sigma_x = \sigma_h + \dfrac{3K_1}{4\sqrt{\pi r}} \\ \sigma_y = \sigma_v + \dfrac{K_1}{4\sqrt{\pi r}} \\ \tau_{xy} = -\dfrac{K_1}{4\sqrt{2\pi r}} \end{cases} \tag{12}$$

where σ_x represents the total stress component along the x-axis; σ_y is the total stress component along the y-axis; and τ_{xy} is the tangential stress. The maximum principal stress (σ_1) on the interface can be calculated by

$$\sigma_1 = \frac{\sigma_x + \sigma_y}{2} + \sqrt{\left(\frac{\sigma_x - \sigma_y}{2}\right)^2 + \tau_{xy}^2} \tag{13}$$

If the maximum principal stress is equal to the tensile strength of the rock in front of the HF tip (T_0), the critical radius r_c of the nonlinear zone can be obtained with $r = r_c$ in Eq. (12).

In previous laboratory experiments and field analysis (Blanton, 1986; Lei et al., 2019; Wu et al., 2021; Zhao et al., 2019; Zhang et al., 2020b), three main intersection modes (crossing, opening, and slippage) were observed between an HF and a stratigraphic interface. Both slippage and opening can result in the termination of HF propagation, and then the internal fluid may flow along the direction of the NF, which further contributes to excessive fluid leakage. Combining the interface model presented in this paper, the critical slippage condition for the interface is

$$|\tau| \geq C + f\sigma_N \tag{14}$$

where C is the cohesion of the interface, and f is the friction coefficient of the interface.

As the fluid pressure within the HF is greater than the total normal stress on the interface, the interface between the two different formations can be dilated, which causes the HF to propagate along the stratigraphic interface. This kind of HF behavior can be formulated by

$$\sigma_N \leq P_{HF} \tag{15}$$

where P_{HF} represents the fluid pressure inside the HF.

In reality, due to HF tip singularity, a critical point can be found near the crack tip satisfying the condition $\sigma_1 = T_0$. Therefore, theoretically, crossing can occur regardless of whether the interface slips or opens. However, once slippage or dilation occurs before crossing, the stress field at the interface can be changed dramatically, which may disturb the subsequent crossing behavior (Zhao et al., 2019). Therefore, crossing becomes the last behavior to be considered after slippage and dilation. In other words, the HF will cross the stratigraphic interface in the case of no slippage and no dilation at the interface, which can be expressed as

$$\begin{cases} \sigma_1 = T_0 \\ |\tau| \leq C + f\sigma_N \\ \sigma_N \geq P_{HF} \end{cases} \tag{16}$$

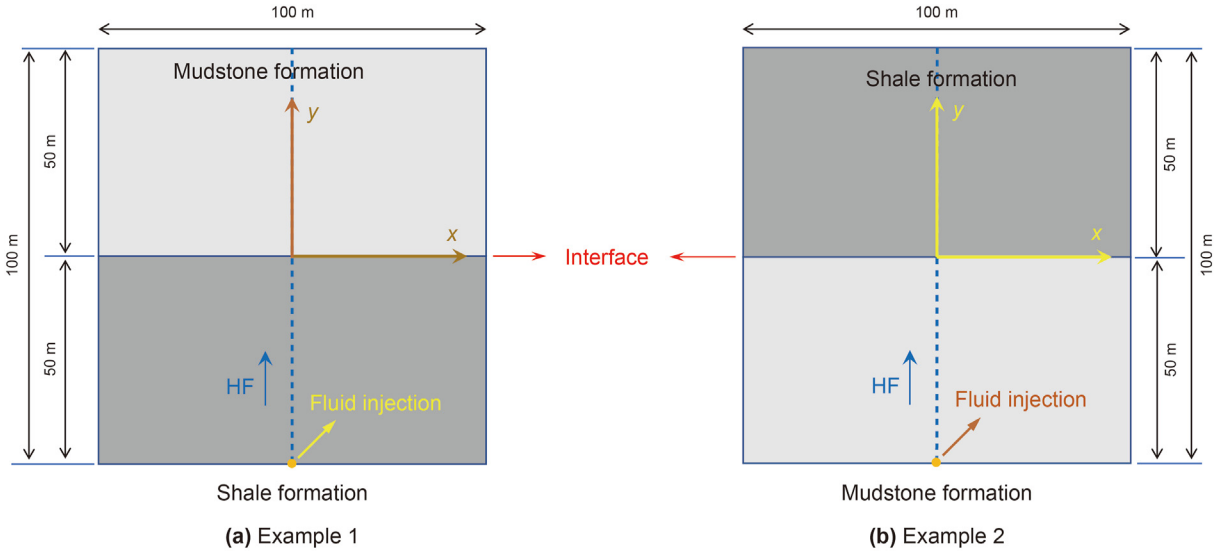

Fig. 2. CZM numerical model of composite rock mass.

Table 1
Basic parameters of CZM simulation.

Physical parameter	Shale (Zhao et al. 2022a)	Mudstone (Zhao et al., 2007)
Elastic modulus E, GPa	22.9	4.9
Poisson's ratio v	0.36	0.17
Tensile strength T_0, MPa	3.36	0.569
Cohesion C, MPa	15.77	2.99
Friction angle φ, degree	38.97	30.3
Fracture toughness, MPa $m^{1/2}$	1.0	0.87
Permeability coefficient k, m/s	1×10^{-7}	1×10^{-8}
Leak-off coefficient m	1×10^{-14}	1×10^{-14}
Void ratio	0.1	0.1
Fluid volumetric weight, N/m^3	9800	

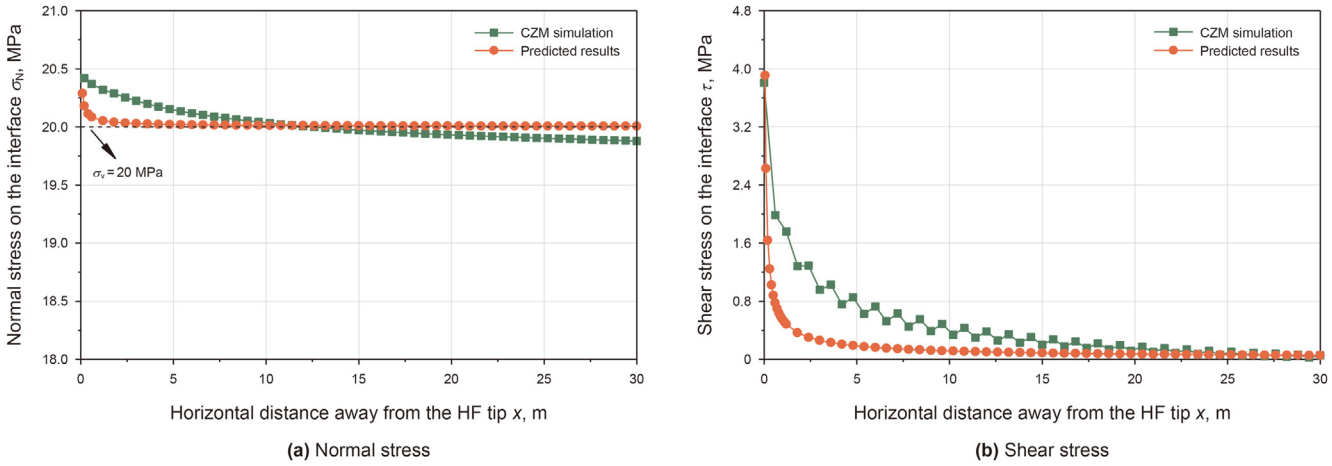

Fig. 3. Example 1: Comparison of normal and shear stress fields on the interface between the presented model and CZM simulations.

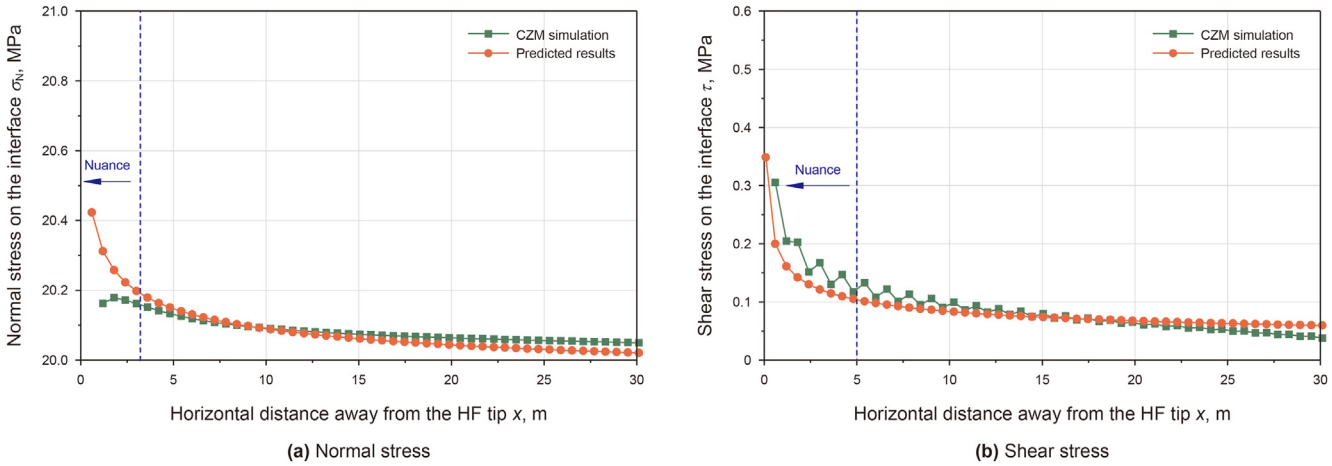

Fig. 4. Example 2: Comparison of normal and shear stress fields on the interface between the presented model and CZM simulations.

3. Validation

3.1. Comparison to numerical simulation results

The Mode I bilinear cohesive zone model (CZM) has been widely applied to model a single crack tip and describe crack nucleation and pervasive cracking for various time or length scales in elastic solids (Elices et al., 2001; Park and Paulino, 2011; Peng et al., 2021). In a CZM, the fracture process zone is lumped into the fracture line and is characterized by a traction-separation law that depends on material properties, which essentially eliminates the stress singularity ahead of the fracture tip and improves the solution convergence of the equations derived from LEFM (Dahi Taleghani et al., 2018; Khoramishad et al., 2010). However, according to Lecampion et al. (2018), the CZM approach possesses some inevitable restrictions in simulating HF problems: (i) the direction of fracture propagation in the CZM must be known or actively updated during propagation; (ii) the simulated fracture morphology is highly dependent on the meshing accuracy; and (iii) an improper mesh will result in bias in the fracture propagation direction as the

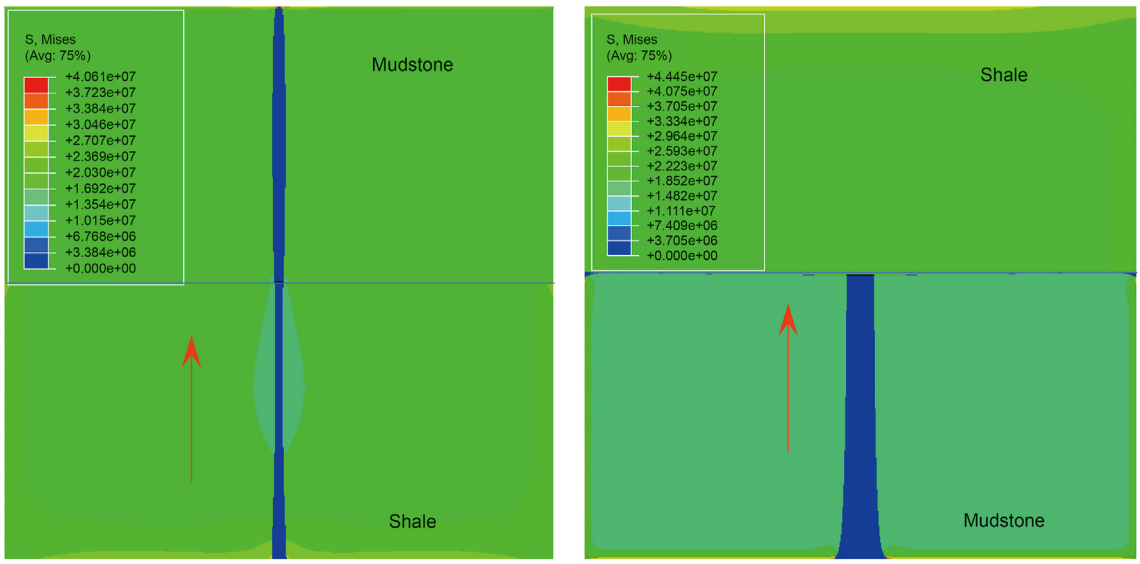

(a) Example 1 (Crossing) **(b)** Example 2 (Arrested)

Fig. 5. Final HF propagation behavior based on CZM simulations.

Table 2
Related calculation parameters from interface model of composite rock mass.

Parameter	Example 1		Example 2		Remarks
	Lower shale	Upper mudstone	Lower mudstone	Upper shale	
Elastic modulus E, GPa	22.9	4.9	4.9	22.9	Zhao et al. (2007, 2022a)
Poisson's ratio v	0.36	0.17	0.17	0.36	
Shear modulus μ, GPa	8.4191	2.0940	2.0940	8.4191	$\mu_j = \frac{E_j}{2(1+v_j)}$
κ	1.56	2.32	2.32	1.56	$\kappa_j = 3 - 4v_j$
α	−0.6782		0.6782		Eq. (8)
β	−0.2984		0.2984		Eq. (8)
λ	0.32		0.69		Eq. (A.33)
Δ_1	0.2919		1.0012		Eq. (B.5)
b	−0.8644		−0.0545		Eq. (B.7)
c	1.8507−0.0001i		0.5411 + 0.0024i		Eq. (B.8)
$\sigma_{\theta 1} + i\tau_{r\theta 1}$	0.0697 + 0.6331i		0.4894 + 0.1706i		Eq. (9)
$\sigma_N - P_{HF}$	>0		<0		Table 1
$\lvert\tau\rvert - (C + f\sigma_N)$	<0		<0		
$\sigma_1 - T_0$	>0		<0		
HF behavior	Crossing		Arrested		

fracture extends to an unknown fracture path. Since the focus of this section is the prediction of HF behavior at the formation interface rather than the investigation of fracture initiation and propagation characteristics before or after the intersection, the fracture trajectory is actually determined (approximated by a cohesive element along the HF propagation direction) before the simulation. Under this circumstance, the CZM allows direct integration along the preset fracture boundary, and the high mesh dependency caused by cohesive element edges is largely avoided, which significantly reduces the computational costs. Therefore, the CZM approach is employed to verify the applicability of the interface model of the composite rock mass by comparing the prediction outcomes to CZM simulation results under the same conditions. Two numerical models considering reservoirs of different combinations of shale and mudstone (Example 1 and Example 2) are constructed, as shown in Fig. 2. The interface and HF are simulated by cohesive elements (delineated by the blue solid and dashed lines in Fig. 2, respectively), and the linear traction-separation relationship defines the critical conditions for crack initiation and propagation. The displacements of the upper and lower sides are fixed in the y-axial direction, and the displacements of the left and right sides are fixed in the x-axial direction. The vertical and horizontal *in-situ* stresses are 20 and 13 MPa, respectively. For each simulation, the fluid is injected at a constant flow rate of 0.01 m^2/s. The physical

Table 3
Basic parameters of Jiang et al.'s experiment (2019).

Material parameter	Tensile strength T_0, MPa	Fracture toughness K_{IC}, MPa $m^{1/2}$	Poisson's ratio v	Porosity ϕ, %	Elastic modulus E, GPa	Permeability K, 10^{-15} m^2
Cement	4.56	0.98	0.19	7.9	6.58	0.0039
Coal	1.69	0.2	0.23	8.9	3.48	0.014–0.20

Table 4
Comparison between Jiang et al.'s (2019) experimental observations and prediction results from the interface model of composite rock mass.

σ_v, MPa	σ_h, MPa	r_c, 10^{-5} m	f	λ	$x_{critical}$, m	Experimental observations	Prediction results
6	3	1.7735	0.72	0.38	0.0024	No crossing	Dilated
7	3	1.1847	0.72	0.38	0.0020	No crossing	Dilated
8	3	0.8469	0.72	0.38	0.0018	No crossing	Slippage
9	3	0.6353	0.72	0.38	0.0016	Crossing	Crossing
6	3	1.7735	0.4976	0.38	0.0024	No crossing	Dilated
7	3	1.1847	0.4976	0.38	0.0020	No crossing	Dilated
8	3	0.8469	0.4976	0.38	0.0018	No crossing	Slippage
11	3	0.3951	0.4976	0.38	0.0013	Crossing	Crossing
11	3	0.3951	0.2557	0.38	0.0013	No crossing	Slippage
12	3	0.3233	0.2557	0.38	0.0012	No crossing	Slippage
13	3	0.2693	0.2557	0.38	0.0011	No crossing	Slippage
14	3	0.2278	0.2557	0.38	0.0011	No crossing	Slippage
15	3	0.1952	0.2557	0.38	0.0010	Crossing	Crossing

parameters of the shale and mudstone formations employed for simulation are summarized in Table 1.

In Example 1 (Fig. 2a), with the known parameters in Table 1, the total normal and shear stresses on the interface can be analytically calculated by combining Eqs. (7)–(10) and numerically obtained by CZM simulation. The stress comparison outcomes are displayed in Fig. 3. Due to the symmetry of the numerical model, it is appropriate to merely consider the stress on the right side of the interface (i.e., $x > 0$).

Fig. 3a depicts the comparison of the normal stress between the CZM simulated results and the predictions of the interface model. Whether in the CZM simulation or analytical prediction, the normal stress decreases with increasing horizontal distance x. In addition, the stress increases toward the HF tip ($x = 0$). This phenomenon can be attributed to the crack-tip stress singularity, as introduced by Renshaw and Pollard (1995). However, the increase in normal stress in the CZM tends to decrease in the vicinity of the HF tip ($x = 0$), contrary to the considerable increase in stress derived by the interface model. This result can be explained by the assumption of the linear traction–separation relationship of CZM that maximally weakens the stress singularity at the HF tip. In this regard, the results of the interface model are capable of better reflecting the stress state of the HF tip compared to the CZM simulation results. From Fig. 3b, we show a similar shear stress variation trend. However, some subtle disparities can also be discerned in the shear stress curves: the shear stress magnitude in the interface model drops more significantly and quickly than that in the CZM simulation with the equal increment of the horizontal distance x. In theory, the singularity at the HF is enhanced due to the combined effect of the interface between two different materials (Akisanya and Meng, 2003; Ming-Yuan and Hutchinson, 1989; Zhao et al., 2022b). Therefore, the CZM results can reflect the issues related to HF initiation and propagation but cannot represent this kind of interface effect, further illustrating the advantage and necessity of using the newly derived interface model.

For further validation, a simulation model consisting of upper shale and lower mudstone (Example 2 in Fig. 2b) was also developed, and the obtained results were compared to the calculated outcomes of the above interface model. Fig. 4 shows the normal and shear stress comparisons under the same parametric conditions (Table 1). Compared to Example 1, a similar difference in the normal and shear stresses between the CZM simulation and model prediction results is identified in Example 2. However, the stress curves almost coincide except for some nuance of the singularity (in $x \leq 3$ m for normal stress and $x \leq 5$ m for shear stress) around the intersection point (O).

Fig. 5 shows the simulation results and the corresponding Mises stress distribution. In Example 1 (upper mudstone and lower shale), the HF crosses the interface after the HF tip reaches the stratigraphic interface (Fig. 5a). Nevertheless, after exchanging the material properties of the upper and lower layers, the HF propagation is arrested by the interface, as shown in Fig. 5b. This HF behavior is consistent with the prediction results of the interface model in Table 2. Therefore, it is reasonable to infer that such an interface model of a composite rock mass is suitable for predicting the behavior of an HF at the stratigraphic interface.

Table 5
Mechanical properties of specimens used for AlTammar et al.'s experiment (2019).

Sample No.	Sample composition (mass fraction), %			E, MPa	K_{IC}, MPa m$^{1/2}$	T_0, MPa
	Plaster	Talc	Hydrostone			
1	40	60	0	124.11	0.037	2.25
2	60	40	0	268.91	0.075	0.69
3	80	20	0	579.18	0.113	1.21
4	100	0	0	1137.68	0.166	2.25
5	80	0	20	1889.23	0.203	2.48
6	60	0	40	2730.42	0.256	2.90
7	40	0	60	4061.16	0.297	4.15
8	20	0	20	4860.98	0.352	4.69
9	0	0	100	6336.51	0.398	6.23

3.2. Comparison to laboratory experiments

In this section, we turn to previously published laboratory evidence to verify the applicability of the interface model of composite rock masses. Three independent experiments were employed for validation based on the works of Jiang et al. (2019), AlTammar et al. (2019), and Ham and Kwon (2020).

3.2.1. Jiang et al.'s experiment

Jiang et al. (2019) performed triaxial hydraulic fracturing experiments adopting coal-rock blocks with different friction coefficients. In accordance with Jiang et al. (2019), the cohesion of the formation interface is assumed to be zero. Other parameters used in Jiang et al.'s (2019) experiment are summarized in Table 3.

Table 4 lists the summary of the experimental observations from Jiang et al. (2019) and the calculation outcomes from the interface model. A restriction to the validity of LEFM is the condition that the plastic deformation can be confined to a small nonlinear zone at the HF tip encompassed by the stress singularity (Llanos et al., 2017). Therefore, the critical radius (r_c) of the nonlinear zone ahead of the HF tip is also summarized in Table 4. Considering the effect of the stress singularity at the HF tip, the critical position ($x_{critical}$) is assumed to be the distance from the HF tip to the interface where a new HF crosses the interface ($\sigma_1 = T_0$), in line with Zhao et al.

Table 6
Comparison between AlTammar et al.'s (2019) experimental observations and prediction results from the interface model of composite rock mass.

Propagating layer	Bounding layer	r_c, m	$x_{critical}$, m	Experimental observations	Prediction results
3	2	0.005	0.0276	Crossing	Crossing
3	6	0.0019	0.0025	Crossing	Crossing
3	5	0.0017	0.0023	Crossing	Crossing
3	7	0.0012	0.0014	Crossing	Crossing
2	5	0.00049	0.00056	Crossing	Crossing
4	7	0.0012	0.0014	**Crossing**	**Dilated**
3	5	0.0017	0.0023	Crossing	Crossing
2	4	0.0014	0.002	Crossing	Crossing
4	6	0.0019	0.0025	Crossing	Crossing

Table 7
Basic parameters of Ham and Kwon's experiment (2020).

Parameter	Fracture toughness K_{IC}, kPa $m^{1/2}$	Poisson's ratio v	Elastic modulus E, kPa
Low stiffness	0.40	0.5 (incompressible)	38
Medium stiffness	1.33		90
High stiffness	1.53		110
Very high stiffness	3.19		283

Table 8
Comparison between Ham and Kwon's (2020) experimental observations and prediction results from the interface model of composite rock mass.

Propagating layer	Bounding layer	No.	r_c, 10^{-6} m	$x_{critical}$, 10^{-5} m	First observations	Prediction results
Medium stiffness	Low stiffness	M-2-L	0.9276	0.8275	Crossing	Crossing
	Medium stiffness	M-2-Ma	8.3718	7.4684	Dilated	Dilated
		M-2-Mb	8.3718	7.4684	**Crossing**	**Dilated**
		M-2-Mc	8.3718	7.4684	Dilated	Dilated
	High stiffness	M-2-H	15.080	13.452	Dilated	Dilated
	Very high stiffness	M-2-VH	94.400	84.210	Dilated	Dilated

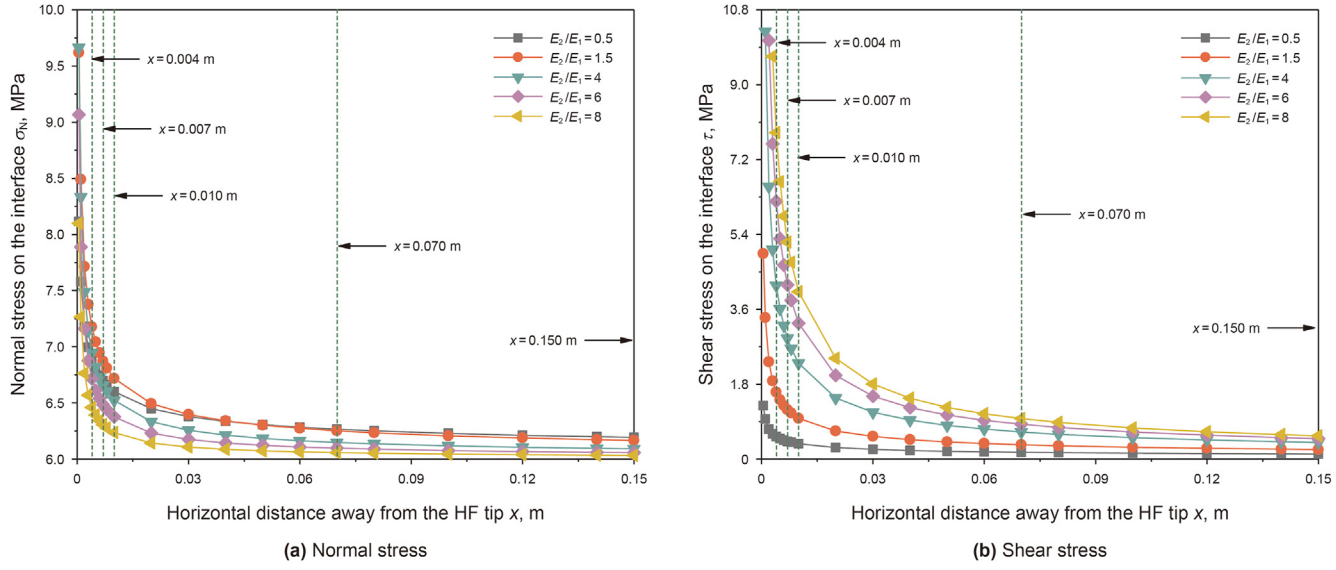

Fig. 6. Normal and shear stress distributions on the interface under different elastic moduli.

(2019). $x_{critical}$ is obtained by combining Eqs. (9)–(13). To ensure the validity of the LEFM, the calculation point mentioned in the above interface model should be outside the nonlinear zone, i.e., $x_{critical} \geq r_c$.

Note that the predictions of "dilation" and "slippage" both belong to the "no crossing" case following the critical stress conditions in the interface model. In this regard, the prediction outcomes of the interface model show good agreement with the experimental results, as illustrated in Table 4. This consistency is a good evidence of the reliability of the newly developed interface model. Furthermore, although the theoretical prediction of the experimental observations has already been compared by Jiang et al. (2019) using their model, the newly presented interface model can provide a more specific evaluation of the HF behavior in the case of no crossing (i.e., slippage or dilation). It is widely accepted that the HF will either move forward (crossing) or be

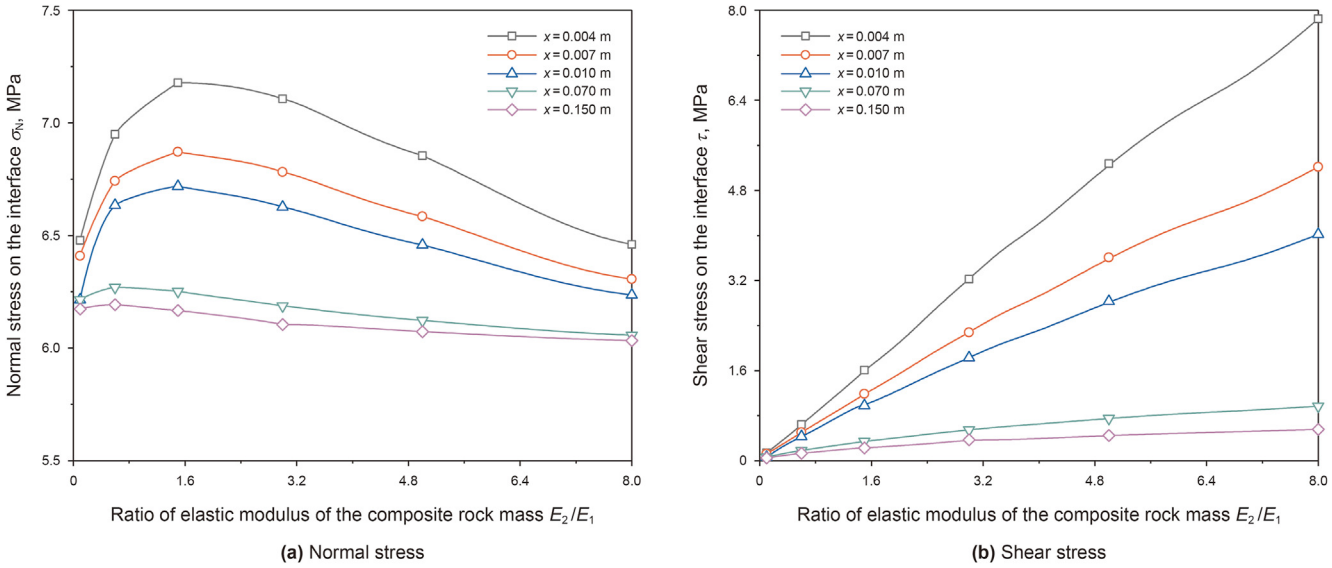

Fig. 7. Normal and shear stress variations with the increase in E_2/E_1 at several fixed locations.

arrested (no crossing) when reaching the interface. However, where and how the HF is arrested or terminated by the interface remains unknown. This difficulty, to a large extent, restricts the development of hydraulic fracturing construction designs. Thus, it is necessary to specify the possible HF behavior in the case of no crossing, especially for HF growth in the composite rock mass.

3.2.2. AlTammar et al.'s experiment

AlTammar et al. (2019) reported numerous hydraulic fracturing tests based on a fracture cell that enables direct observation of fracture growth near material interfaces. Different layered specimens (154.4 × 152.4 × 3.2 mm^3 in size) were cast by mixing talc with plaster to make softer materials and mixing hydrostone with plaster to simulate harder materials (reservoirs), which created known contrasts in layer properties between adjacent layers. All specimen mixtures had an approximately constant Poisson's ratio between 0.22 and 0.25 according to AlTammar et al. (2019). For the convenience of calculation, Poisson's ratio is taken as 0.23. Other mechanical properties of these rock-like specimens are shown in Table 5. In addition, a 0.45 MPa far-field stress was applied parallel to the specimen's long side in the horizontal direction, and the other long side was unconfined in the vertical direction. The HF growth was captured by a high-resolution digital camera in real time, facilitating the estimation of HF behavior at the interface.

Table 6 summarizes AlTammar et al.'s experimental results and the predictions based on the interface model of the composite rock mass. The highlighted cells show the mismatch cases between the experimental observation and prediction outcomes. It is clear that only one inconsistent case is found in Table 6, which indicates that the experimental observations generally agree well with the model's predictions.

3.2.3. Ham and Kwon's experiment

Ham and Kwon (2020) simulated the hydraulic fracturing process of an HF crossing an orthogonal discontinuity between materials of different stiffnesses. Photoelastic, transparent, and soft (or deformable) gelatin was chosen as analogs to soft reservoir rocks, which allowed direct observation of the HF propagation state and interaction behavior. The material properties of the gelatin samples are summarized in Table 7. Table 8 lists the comparison between Ham and Kwon's (2020) experimental observations and the prediction outcomes from the interface model of the composite rock mass. Overall, the calculation outcomes obtained from the interface model of the composite rock mass show good agreement with the experimental results except for the M-2-Mb test (highlighted in bold font in Table 8).

Reviewing the results of the three experiments in Tables 4, 6 and 8, we observed two inconsistent cases in total. According to Zhao et al. (2019), the mismatch can be attributable to the existence of nonlinear (plastic) zones and the combined action of the stress singularity ahead of the fracture tip, which can induce either softening or hardening inside the nonlinear region of the rock. Then, the actual radius of the nonlinear region is changed so that the initial linear elastic stress assumption about r_c (i.e., $r > r_c$) is invalid, thus leading to inconsistent cases. Nonetheless, the inconsistent cases are in an acceptable range. Therefore, the developed model can reliably predict the HF penetration and termination behavior at the interface between two layers with different mechanical properties.

4. Parametric sensitivity analysis

This section presents a parametric sensitivity analysis to explore the influence of the related parameters in the interface model of the composite rock mass (i.e., elastic modulus, Poisson's ratio, and fracture toughness). The control variable method was adopted by successively and independently varying a parameter while other parameters remained constant. For convenience, we chose the physical parameters from Jiang et al.'s experiment (2019) for calculating and analyzing the stress field within the interval range of (0, 0.15 m) on the interface. The vertical and horizontal *in-situ* stresses are kept constant at $\sigma_v = 6$ MPa and $\sigma_h = 3$ MPa, respectively.

4.1. Influence of the elastic modulus

The normal and shear stress distributions on the interface under different ratios of elastic modulus are plotted in Fig. 6, respectively. Note that the origin of the coordinates in Fig. 6 is consistent with the intersection point (*O* in Fig. 1) between the HF and the interface. Despite the influence of elastic modulus, the stress value approaches infinity at the HF tip; then, with the increase in the

horizontal distance x, the stress decreases. In addition, enlarging the difference in elastic modulus between Formation 2 and Formation 1 (expressed by a dimensionless ratio E_2/E_1) generally results in a reduction in the normal stress (especially for $E_2/E_1 > 1.5$) and a rise in the shear stress, but does not change the overall stress distribution law.

For the convenience of comparison, the stress values at the horizontal distance (x) of 0.004, 0.007, 0.01, 0.07, and 0.15 m were extracted and plotted in another form, as shown in Fig. 7. With the increase in E_2/E_1, the normal stress first increases and then decreases (Fig. 7a), implying that the normal stress is a nonmonotonic function of the elastic modulus contrast. This effect appears to be more prominent at a location closer to the HF tip ($x < 0.01$ m). Amid this range, the normal stress approximates its maximum at $E_2/E_1 = 1.5$, which represents the optimal elastic modulus combination of the composite rock mass that generates the maximum normal stress component on the interface. Fig. 7b displays the continuous increasing tendency of shear stress with the increase in elastic modulus contrast, which reveals that the shear stress is positively correlated with the modulus contrast.

Fig. 8 exhibits how the HF extends under the influence of stress difference and modulus contrast at the friction coefficient of 0.2557, 0.4976 and 0.72, respectively. Overall, different friction coefficients will change the geometry of the critical slippage curves and affect HF behavior (crossing or slippage). In the case of fixed friction coefficient (e.g., $f = 0.4976$), the effect of modulus contrast between adjacent layers can be disturbed by the magnitude of stress difference. For a high stress difference (e.g., $\Delta = 5$), the crossing scope accounts for a larger proportion than opening and slippage at higher E_2/E_1, which indicates that increasing the modulus ratio (E_2/E_1) will facilitate the occurrence of crossing. With the decrease in the stress difference, the crossing range of E_2/E_1 also decreases. When the stress difference is relatively low (e.g., $\Delta = 0.2$), the stratigraphic interface is likely to be dilated by the HF despite changing E_2/E_1. These results are consistent with the observations of hydraulic fracturing experiments (Abe et al., 2021; Zhou et al., 2008).

According to the *in-situ* stress data reported by Zhao et al.

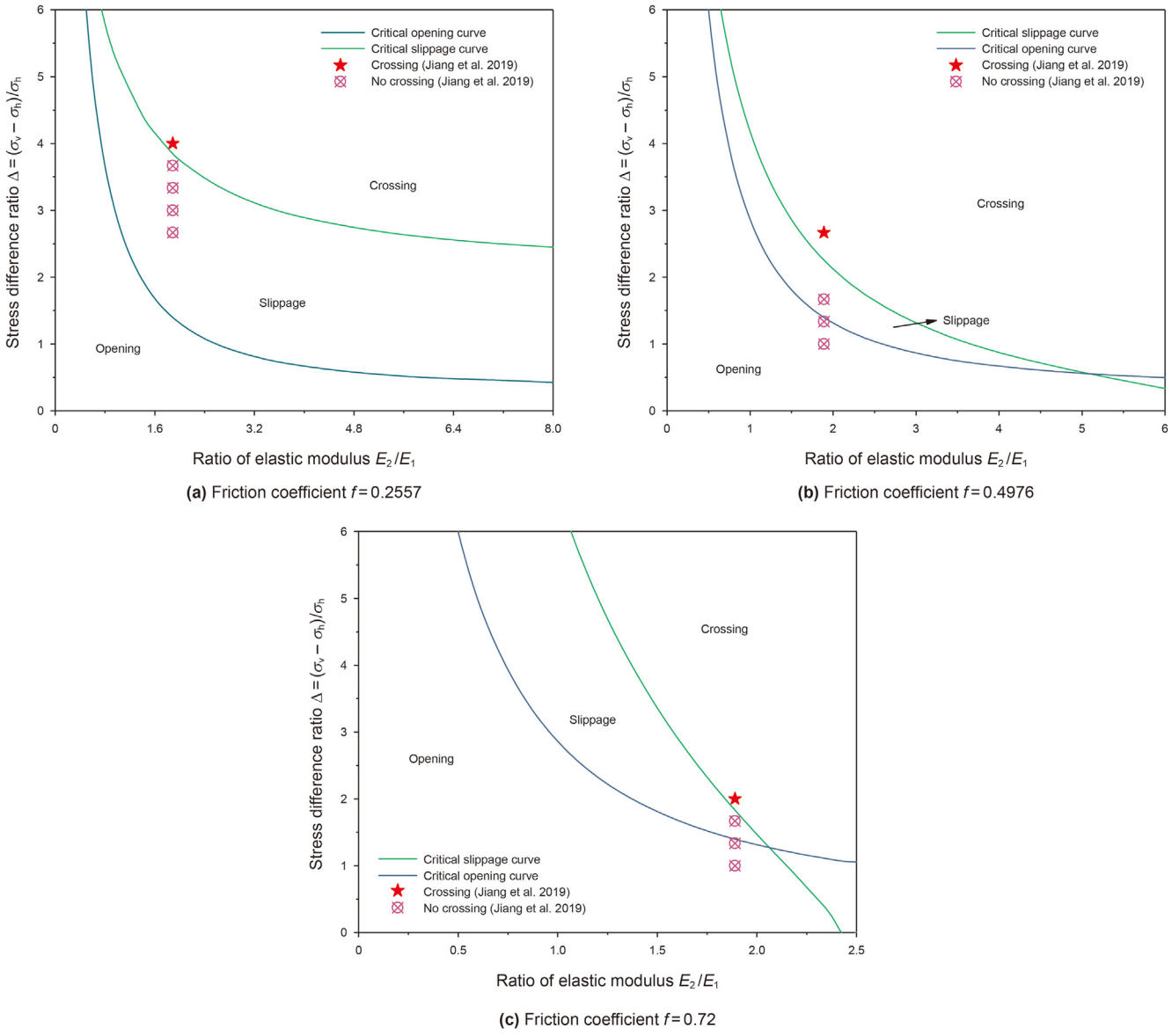

Fig. 8. Critical opening and slippage curves for vertical HF propagation behaviour based on Jiang et al.'s experiment (2019).

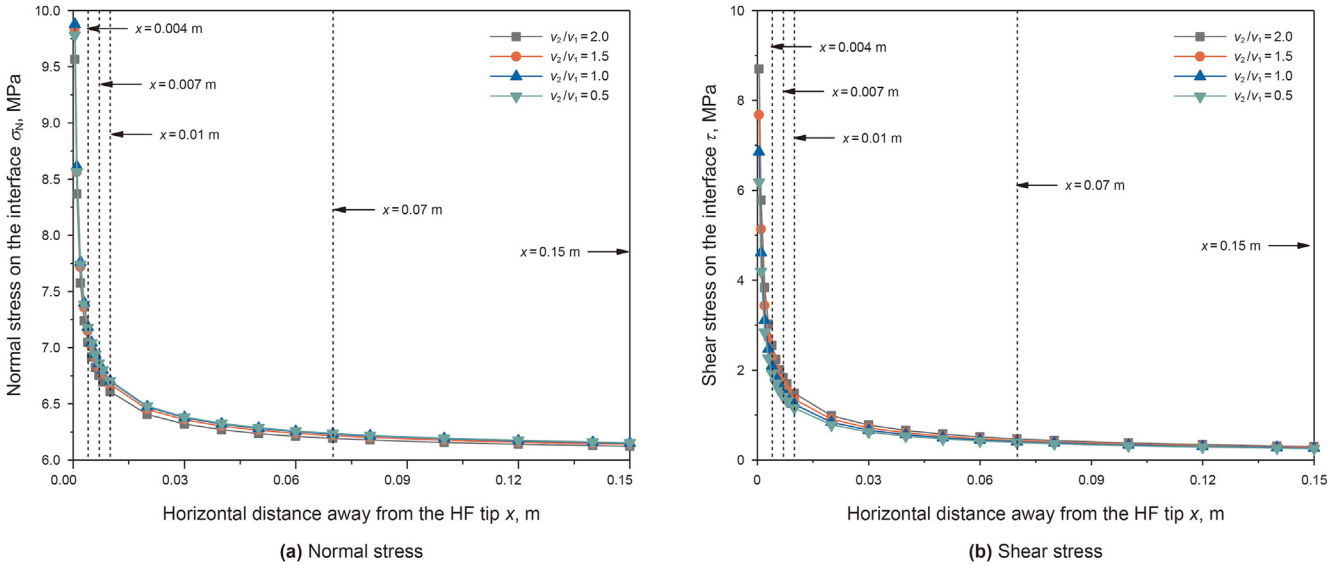

Fig. 9. Normal and shear stress distributions on the interface under different Poisson's ratios.

(2007), the practical stress difference ratio (Δ) was generally less than 0.8 in most parts of China. This range is partly aligned with the crossing stress scope at $f = 0.4796$ (for $E_2/E_1 = 4–6$) in Fig. 8b, which demonstrates the model's validity for predicting the occurrence of crossing under practical stress conditions. In fact, the stress difference ratio in Fig. 8 only presents a theoretical evaluation of HF behavior based on particular friction coefficients tested by Jiang et al. (2019) in the laboratory. Some inconsistency may appear when these results are directly applied to engineering practice. Nevertheless, the current results can still illustrate that the influence of elastic modulus on HF behavior at the interface is easily disturbed by the *in-situ* stress difference.

4.2. Influence of Poisson's ratio

To investigate the effect of Poisson's ratio on HF behavior, we defined a dimensionless parameter v_2/v_1 to characterize the relative magnitudes of the Poisson's ratios of the upper and lower formations. The allowable range of Poisson's ratio for an elastic material in the geostress field is from 0 to 0.5 (Ciambella et al., 2015). With fixed $v_1 = 0.23$, the value of v_2/v_1 ranges from 0.5 to 2. Fig. 9 shows the normal and shear stress distribution on the layer interface's right side ($x \geq 0$). Fig. 9 also shows that the variation in Poisson's ratio mainly changes the stress value and hardly alters the geometry of the stress distribution curves. In addition, both normal and shear stresses remain approximately constant under different Poisson's ratios, differing from the influence of the elastic modulus on the stress value. Fig. 10 shows the variation in the stress value at certain designated locations outlined in Fig. 9. The normal stress decreases slightly with increasing v_2/v_1, while the shear stress considerably increases. Moreover, both the normal and shear stress values are sensitive to the distance (x) from the HF tip. This kind of sensitivity is primarily manifested by the variation in the stress value: closer to the HF tip, the impact of Poisson's ratio on the stress

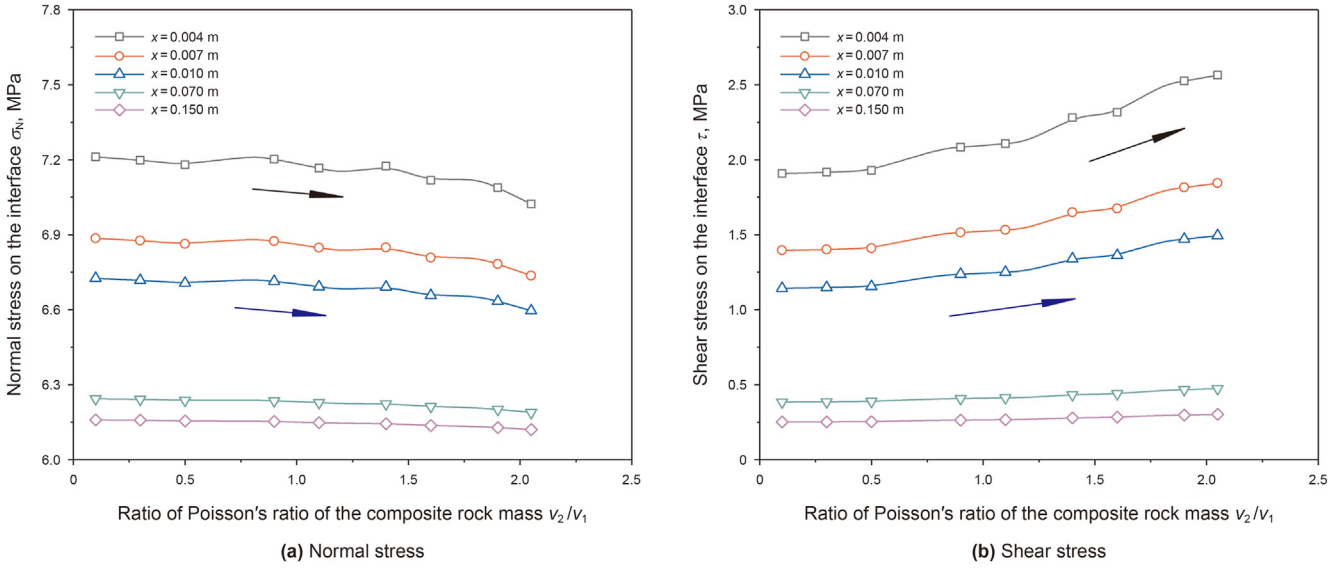

Fig. 10. Normal and shear stress variations with the increase of v_2/v_1 at several fixed locations.

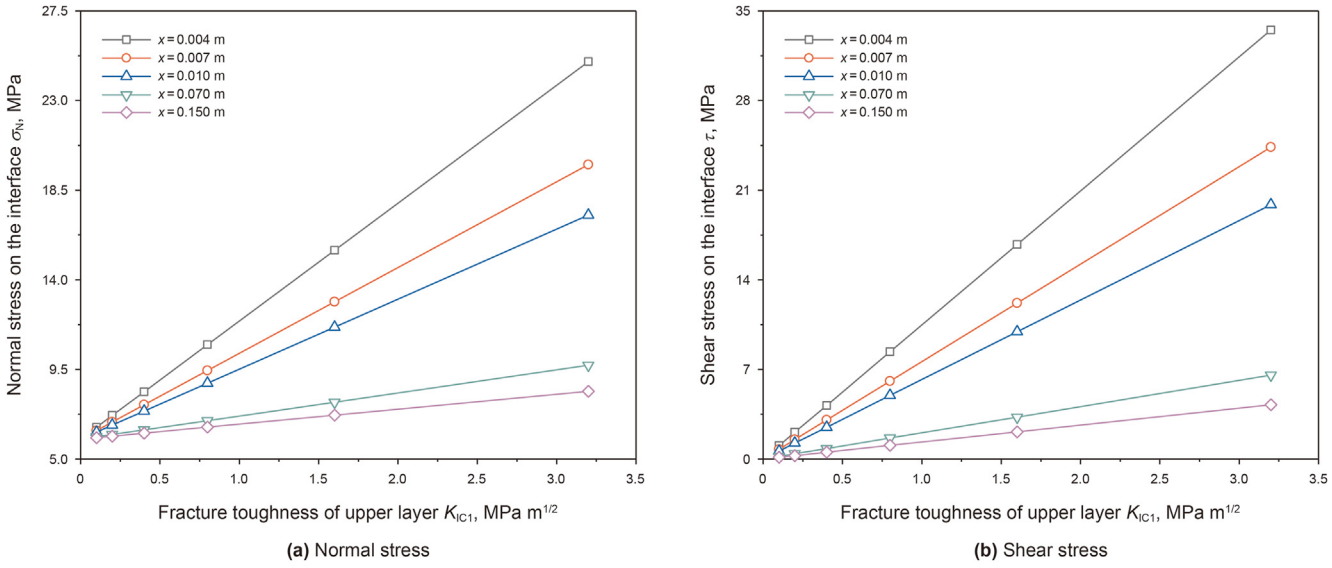

Fig. 11. Normal and shear stress variations with the increase of K_{IC1} at several designated locations.

value is more prominent. But at a location away from the HF tip ($x > 0.07$ m), the effect of Poisson's ratio gradually weakens.

Generally, Poisson's ratio has a minor effect on changing the stress distribution at the interface. Compared to the elastic modulus, Poisson's ratio may not be a dominant factor in HF height containment.

4.3. Influence of fracture toughness

The fracture toughness of a material essentially reflects the critical initiation capacity of a new crack during the rock fracturing process. In this section, the influence of the fracture toughness (K_{IC1}) of Formation 1 (target layer of the propagating HF) was analyzed by varying K_{IC1} from 0.1 to 3.2 MPa m$^{1/2}$. Meanwhile, the fracture toughness (K_{IC2}) of Formation 2 (pay zone layer initially containing the HF) remains constant at 0.98 MPa m$^{1/2}$.

As shown in Fig. 11, the normal and shear stresses exhibit linear relationships with K_{IC1}. Eq. (9) can partly explain this relationship, which shows a linear correlation of the fracture toughness (critical stress intensity factor) with the induced stress field ahead of the HF tip. At the same location (horizontal distance x) of 0.004, 0.007, 0.001, 0.07, or 0.15 m), the larger the fracture toughness is, the greater the normal and shear stresses are projected at the interface. Due to the stress singularity at the HF tip, a similar location-related variation in the stress value can also be found despite the effect of fracture toughness: the stress increases toward the HF tip.

Compared to the normal stress, the fracture toughness (K_{IC1}) appears to have a more significant effect on the shear stress. Specifically, at the location $x = 0.004$ m, as the fracture toughness changes from 0.2 to 0.4 MPa m$^{1/2}$, the normal stress increases from 7.18 to 8.36 MPa (increased by only 16.4%), and the shear stress increases from 2.09 to 4.19 MPa (almost doubling). Hence, increasing the fracture toughness of the bounding layer (K_{IC1}) can produce more shear stress components on the interface and promote the occurrence of slippage. This conclusion, to some degree, contradicts our previous findings in Zhao et al. (2019) that increasing the fracture toughness can inhibit the slippage behavior. However, it should be noted that a homogeneous medium (one rock material) is concerned in Zhao et al. (2019). These inconsistent results may come from the combined effect of two different rock materials with an interface in the current model, which changes the singularity state of the HF tip and facilitates the occurrence of slippage on the interface (Liu et al., 2021; Lu et al., 2015).

4.4. Comparison of the influence of the three parameters

One location (0, 0.004 m) near the fracture tip was chosen to compare the influence degree of the three parameters (elastic modulus, Poisson's ratio, and fracture toughness). Fig. 12a and b shows the normal and shear stresses at this location under different ratios of the three parameters (i.e., E_2/E_1, ν_2/ν_1, and K_{IC2}/K_{IC1}). Clearly, the fracture toughness contrast between adjacent layers appears to be the most dominant parameter influencing the normal and shear stress values, the elastic modulus ranks second, and Poisson's ratio has the minimal impact on the stress. With the increase in the corresponding dimensionless ratio, the effect of the fracture toughness contrast on the shear stress weakens. In contrast, the elastic modulus contrast gradually dominates the variation in the shear stress. This result indicates that when the mechanical properties (fracture toughness and elastic modulus) of the bounding layer are greater than those of the pay zone layer, the interface is more likely to be affected by the fracture toughness contrast; otherwise, the interface is more susceptible to the modulus contrast.

Furthermore, based on the critical slippage condition (Eq. (14)), the effects of the three parameters on the interface's slippage stability can be evaluated by the following equation:

$$F = C + f\sigma_N - |\tau| \tag{17}$$

In accordance with Jiang et al. (2019), the interface cohesion is known ($C = 0$), and the friction coefficient is taken as 0.2557. Then, the slippage stability is analyzed by combining the normal and shear stresses under different ratios of elastic modulus, Poisson's ratio, and fracture toughness. If the function F is less than zero, slippage occurs on the interface. Otherwise, the interface remains stable in the shear direction.

Fig. 12c plots the slippage tendency with increasing dimensionless ratios of the three parameters. Generally, the Poisson's ratio difference between the adjacent layers can only increase the slippage tendency of the formation interface (or increase the shear stress on the interface) but cannot lead to interface slippage (i.e., F is always greater than 0). This result is caused by the range limitation

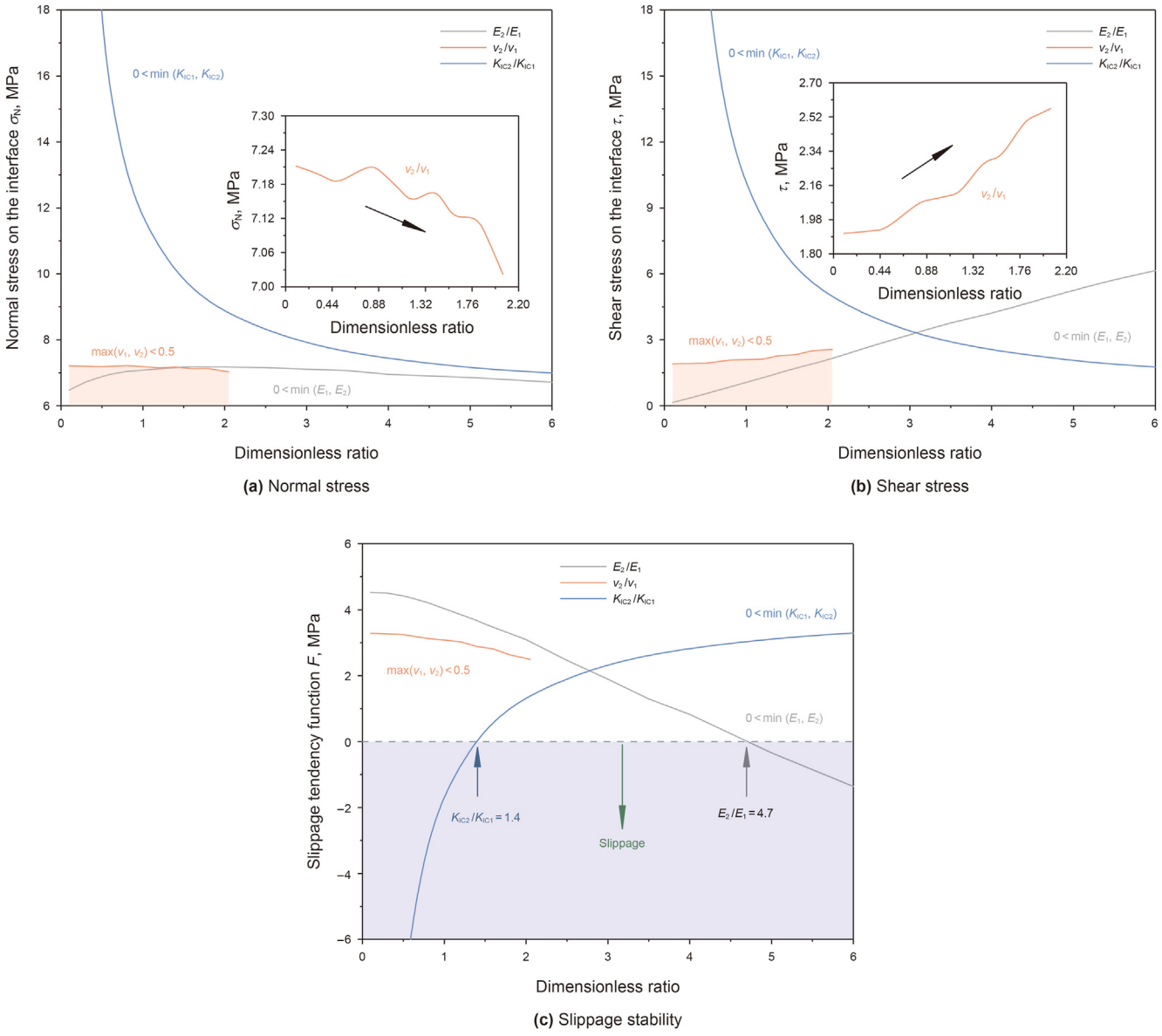

Fig. 12. Comparison of stress variation and slippage stability at the location (0, 0.004 m) with the increase in the dimensionless ratio of elastic modulus, Poisson's ratio, and fracture toughness.

of Poisson's ratio ($0 < v \leq 0.5$), as aforementioned in Section 4.2. In contrast, increasing the elastic modulus of the pay zone layer ($E_2/E_1 > 4.7$) and increasing the fracture toughness of the bounding layer ($K_{IC2}/K_{IC1} < 1.4$) will ultimately cause shear slippage on the interface. Once slippage occurs, the growth of the HF will likely terminate, and no crossing will occur. Therefore, the elastic modulus and fracture toughness are the main parameters that influence HF penetration and termination at the interface.

The higher fracture toughness of the bounding layer restricts the HF from crossing the interface by promoting slippage on the interface, which is consistent with the theoretical inference of Thiercelin et al. (1989) and the experimental observation of Xing et al. (2018). For the elastic modulus, it has been well documented that a fracture will theoretically be arrested when propagating from a lower-modulus layer toward a higher-modulus layer (Simonson et al., 1978). However, some numerical studies (Gu and Siebrits, 2008) and field evidence (Wolhart et al., 2004) show that low-modulus bounding layers can contain the growth of the HF height. In Fig. 12c, it can also be observed that the lower elastic modulus of the bounding layer (i.e., higher E_2/E_1) increases the possibility of shear slippage on the interface and thus prevents the HF from crossing the interface. This contradictory influence of the modulus contrast can be attributed to the disturbance of the magnitude of stress difference that probably reduces the impact of the elastic modulus contrast on the HF growth behavior, as shown in Fig. 8. In this sense, the influence of the elastic modulus contrast on HF growth is complex and easily disturbed by the *in-situ* stress difference. In addition, according to Gu and Siebrits (2008), Warpinski et al. (1982), and Xing et al. (2018), the fracture process zone, fluid viscosity, fracture width, and *in-situ* stress gradients can also hinder the effects of the elastic modulus contrast on HF behavior at the interface. The roles of these parameters, which are not considered in the current theoretical model, clearly must be accounted for in future research. Nonetheless, the results of this parametric study can still be applied to control the HF height growth in formations with varying properties provided that the *in-*

situ stress is kept constant. On the other hand, it is imperative to determine the relative difference in the fracture toughness and elastic modulus between the pay zone and bounding layer in a region where effective fracture containment is desired.

5. Conclusions

In this paper, an interface model of a composite rock mass with an HF orthogonally intersecting a stratigraphic interface was proposed to predict HF penetration (crossing) or termination (dilation or slippage) at the interface. To verify the model's applicability and reliability, comparisons between this model's predictions and CZM simulation results as well as previously published experimental evidence were conducted. A parametric study of the elastic modulus, Poisson's ratio and fracture toughness was presented, and the influence degree of the three parameters was compared. The following conclusions were primarily obtained:

(1) Due to the stress singularity at the HF tip, the normal and shear stresses at the interface decrease away from the HF tip. Compared to the CZM, the new model additionally reflects the changes in the singularity of the HF tip at the interface of two dissimilar materials, which further illustrates the advantage of the presented model. The calculation outcomes obtained from the new model are generally consistent with the experimental data.
(2) With increasing E_2/E_1, the normal stress acting on the interface first increases and then decreases, whereas the shear stress shows a continuously increasing trend, which implies an increasing possibility of slippage. The effect of the elastic modulus contrast on HF growth can be disturbed by stress difference. For a high stress difference, increasing the elastic modulus contrast between adjacent layers will facilitate crossing. However, at a relatively low differential stress, the stratigraphic interface may continue to be dilated by the HF regardless of the changes in E_2/E_1.
(3) The contrast in Poisson's ratio has a minor effect on HF behavior at the formation interface. The normal stress acting on the interface decreases slightly with increasing v_2/v_1, while the shear stress displays an apparent increasing trend.
(4) Compared to the variation in the normal stress, increasing the fracture toughness of the bounding layer (Formation 1) induces more shear stress at the interface, which may further promote interface slipping and thereby restrict the HF from crossing the interface.
(5) Among the three studied parameters, Poisson's ratio exerts the least interference effect on the HF behavior at the stratigraphic interface. When the fracture toughness and elastic modulus of the bounding layer are greater than those of the pay zone layer, the HF growth at the interface is prone to be affected by the fracture toughness contrast; otherwise, the HF growth is more sensitive to the elastic modulus contrast.

Compliance with ethical standards

The authors wish to confirm that this paper did not attract any form of financial support that may have influenced its outcome. Thus, no conflict of interest emanated on the course of its preparation and submission for publication.

Acknowledgments

This research was supported by the National Natural Science Foundation of China (No. 52064006, 52164001 and 52004072), the Guizhou Provincial Science and Technology Foundation (No. [2020] 4Y044, No. [2021]292, No. GCC[2022]005 and [2021]N404), and the China Scholarship Council program (202006050112). In addition, the authors would like to thank the anonymous reviewers for their constructive comments and the editor for review of the manuscript.

Appendix A. Solving the interface eigenvalue λ

To solve the interface eigenvalue λ, we introduced the following matrix functions

$$\boldsymbol{H}(\xi)=\begin{pmatrix} e^{2i\xi} & 0 \\ 0 & e^{-2i\xi} \end{pmatrix},\ \boldsymbol{F}(\xi)=\begin{pmatrix} 0 & e^{-2i\xi} \\ e^{2i\xi} & 0 \end{pmatrix} \tag{A.1}$$

Then, the following relationship holds

$$\boldsymbol{H}(\xi)\boldsymbol{H}(-\xi)=\boldsymbol{I},\ \ \boldsymbol{F}(\xi)\boldsymbol{F}(\xi)=\boldsymbol{I} \tag{A.2}$$

$$\boldsymbol{H}(\xi)\boldsymbol{F}(\delta)=\boldsymbol{F}(\delta-\xi)=\boldsymbol{F}(\delta)\boldsymbol{H}(-\xi) \tag{A.3}$$

$$\boldsymbol{H}(\xi+\delta)=\boldsymbol{H}(\xi)\boldsymbol{H}(\delta)=\boldsymbol{H}(\delta)\boldsymbol{H}(\xi) \tag{A.4}$$

$$\boldsymbol{F}(\xi)\boldsymbol{F}(\delta)=\boldsymbol{F}(-\delta)\boldsymbol{F}(-\xi)=\boldsymbol{H}(-\xi)\boldsymbol{H}(\delta) \tag{A.5}$$

where the symbol $\boldsymbol{I}$ is the unit matrix.

From Eq. (6e), we have

$$\begin{Bmatrix} C_2 \\ D_2 \end{Bmatrix}=-\begin{pmatrix} \lambda & e^{-2i\lambda\pi} \\ e^{2i\lambda\pi} & \lambda \end{pmatrix}\begin{Bmatrix} A_2 \\ B_2 \end{Bmatrix}=-\{\lambda\boldsymbol{I}+\boldsymbol{F}(\lambda\pi)\}\begin{Bmatrix} A_2 \\ B_2 \end{Bmatrix} \tag{A.6}$$

From Eq. (6f), we get

$$\begin{Bmatrix} C_3 \\ D_3 \end{Bmatrix}=-\begin{pmatrix} \lambda & e^{2i\lambda\pi} \\ e^{-2i\lambda\pi} & \lambda \end{pmatrix}\begin{Bmatrix} A_3 \\ B_3 \end{Bmatrix}=-\{\lambda\boldsymbol{I}+\boldsymbol{F}(-\lambda\pi)\}\begin{Bmatrix} A_3 \\ B_3 \end{Bmatrix} \tag{A.7}$$

From Eq. (6a), we obtain

$$\begin{aligned} &\left\{\lambda\boldsymbol{I}+\boldsymbol{H}\left(\frac{\pi}{2}\right)\boldsymbol{F}\left(\frac{\lambda\pi}{2}\right)\right\}\begin{Bmatrix} A_1 \\ B_1 \end{Bmatrix}+\boldsymbol{H}\left(\frac{\pi}{2}\right)\begin{Bmatrix} C_1 \\ D_1 \end{Bmatrix} \\ &=\left\{\lambda\boldsymbol{I}+\boldsymbol{H}\left(\frac{\pi}{2}\right)\boldsymbol{F}\left(\frac{\lambda\pi}{2}\right)\right\}\begin{Bmatrix} A_2 \\ B_2 \end{Bmatrix}+\boldsymbol{H}\left(\frac{\pi}{2}\right)\begin{Bmatrix} C_2 \\ D_2 \end{Bmatrix} \end{aligned} \tag{A.8}$$

From Eq. (6b), we derive

$$\begin{aligned} &\Gamma\left\{\kappa_1\boldsymbol{I}-\lambda\boldsymbol{H}\left(\frac{\pi}{2}\right)\boldsymbol{F}\left(\frac{\lambda\pi}{2}\right)\right\}\begin{Bmatrix} A_1 \\ B_1 \end{Bmatrix}-\Gamma\boldsymbol{F}\left(\frac{\lambda\pi}{2}\right)\begin{Bmatrix} C_1 \\ D_1 \end{Bmatrix} \\ &=\left\{\kappa_2\boldsymbol{I}-\lambda\boldsymbol{H}\left(\frac{\pi}{2}\right)\boldsymbol{F}\left(\frac{\lambda\pi}{2}\right)\right\}\begin{Bmatrix} A_2 \\ B_2 \end{Bmatrix}-\boldsymbol{F}\left(\frac{\lambda\pi}{2}\right)\begin{Bmatrix} C_2 \\ D_2 \end{Bmatrix} \end{aligned} \tag{A.9}$$

From Eq. (6c), we have

$$\begin{aligned} &\left\{\lambda\boldsymbol{I}+\boldsymbol{H}\left(-\frac{\pi}{2}\right)\boldsymbol{H}(\lambda\pi)\boldsymbol{F}\left(\frac{\lambda\pi}{2}\right)\right\}\begin{Bmatrix} A_1 \\ B_1 \end{Bmatrix}+\boldsymbol{H}\left(-\frac{\pi}{2}\right)\begin{Bmatrix} C_1 \\ D_1 \end{Bmatrix} \\ &=\left\{\lambda\boldsymbol{I}+\boldsymbol{H}\left(-\frac{\pi}{2}\right)\boldsymbol{H}(\lambda\pi)\boldsymbol{F}\left(\frac{\lambda\pi}{2}\right)\right\}\begin{Bmatrix} A_3 \\ B_3 \end{Bmatrix}+\boldsymbol{H}\left(-\frac{\pi}{2}\right)\begin{Bmatrix} C_3 \\ D_3 \end{Bmatrix} \end{aligned} \tag{A.10}$$

From Eq. (6d), we obtain

$$\begin{aligned} &\Gamma\left\{\kappa_1\boldsymbol{I}-\lambda\boldsymbol{H}\left(\frac{\pi}{2}\right)\boldsymbol{H}(\lambda\pi)\boldsymbol{F}\left(\frac{\lambda\pi}{2}\right)\right\}\begin{Bmatrix} A_1 \\ B_1 \end{Bmatrix}-\Gamma\boldsymbol{H}(\lambda\pi)\boldsymbol{F}\left(\frac{\lambda\pi}{2}\right)\begin{Bmatrix} C_1 \\ D_1 \end{Bmatrix} \\ &=\left\{\kappa_2\boldsymbol{I}-\lambda\boldsymbol{H}\left(\frac{\pi}{2}\right)\boldsymbol{H}(\lambda\pi)\boldsymbol{F}\left(\frac{\lambda\pi}{2}\right)\right\}\begin{Bmatrix} A_3 \\ B_3 \end{Bmatrix}-\boldsymbol{H}(\lambda\pi)\boldsymbol{F}\left(\frac{\lambda\pi}{2}\right)\begin{Bmatrix} C_3 \\ D_3 \end{Bmatrix} \end{aligned} \tag{A.11}$$

Choosing $(A_3, B_3)^{\mathrm{T}}$ as the only final undetermined coefficient, we can eliminate other coefficients by combining Eq. (6a) – (6f).

We substitute Eq. (A.6) into Eq. (A.8) and obtain

$$\begin{aligned}
&\left\{\lambda\boldsymbol{I}+\boldsymbol{H}\left(\frac{\pi}{2}\right)\boldsymbol{F}\left(\frac{\lambda\pi}{2}\right)\right\}\left\{\frac{A_1}{B_1}\right\}+\boldsymbol{H}\left(\frac{\pi}{2}\right)\left\{\frac{C_1}{D_1}\right\}\\
&=\left\{\lambda\boldsymbol{I}+\boldsymbol{H}\left(\frac{\pi}{2}\right)\boldsymbol{F}\left(\frac{\lambda\pi}{2}\right)\right\}\left\{\frac{A_2}{B_2}\right\}-\boldsymbol{H}\left(\frac{\pi}{2}\right)\{\lambda\boldsymbol{I}+\boldsymbol{F}(\lambda\pi)\}\left\{\frac{A_2}{B_2}\right\}\\
&=\left\{\lambda\left(\boldsymbol{I}-\boldsymbol{H}\left(\frac{\pi}{2}\right)\right)+\boldsymbol{H}\left(\frac{\pi}{2}\right)\boldsymbol{F}\left(\frac{\lambda\pi}{2}\right)-\boldsymbol{H}\left(\frac{\pi}{2}\right)\boldsymbol{F}(\lambda\pi)\right\}\left\{\frac{A_2}{B_2}\right\}
\end{aligned}$$

After multiplying both sides with $\boldsymbol{H}(-\frac{\pi}{2})$, we have

$$\begin{aligned}
\left\{\frac{C_1}{D_1}\right\}&=-\left\{\lambda\boldsymbol{H}\left(-\frac{\pi}{2}\right)+\boldsymbol{F}\left(\frac{\lambda\pi}{2}\right)\right\}\left\{\frac{A_1}{B_1}\right\}\\
&+\left\{\lambda\left(\boldsymbol{H}\left(-\frac{\pi}{2}\right)-\boldsymbol{I}\right)+\boldsymbol{F}\left(\frac{\lambda\pi}{2}\right)-\boldsymbol{F}(\lambda\pi)\right\}\left\{\frac{A_2}{B_2}\right\}
\end{aligned}\tag{A.12}$$

Substitution of Eqs. (A.6) and (A.12) into Eq. (A.9), we get

$$\begin{aligned}
&\Gamma\left\{\kappa_1\boldsymbol{I}-\lambda\boldsymbol{H}\left(\frac{\pi}{2}\right)\boldsymbol{F}\left(\frac{\lambda\pi}{2}\right)\right\}\left\{\frac{A_1}{B_1}\right\}\\
&+\Gamma\boldsymbol{F}\left(\frac{\lambda\pi}{2}\right)\left\{\lambda\boldsymbol{H}\left(-\frac{\pi}{2}\right)+\boldsymbol{F}\left(\frac{\lambda\pi}{2}\right)\right\}\left\{\frac{A_1}{B_1}\right\}\\
&-\Gamma\boldsymbol{F}\left(\frac{\lambda\pi}{2}\right)\left\{\lambda\left(\boldsymbol{H}\left(-\frac{\pi}{2}\right)-\boldsymbol{I}\right)+\boldsymbol{F}\left(\frac{\lambda\pi}{2}\right)-\boldsymbol{F}(\lambda\pi)\right\}\left\{\frac{A_2}{B_2}\right\}\\
&=\left\{\kappa_2\boldsymbol{I}-\lambda\boldsymbol{H}\left(\frac{\pi}{2}\right)\boldsymbol{F}\left(\frac{\lambda\pi}{2}\right)\right\}\left\{\frac{A_2}{B_2}\right\}+\boldsymbol{F}\left(\frac{\lambda\pi}{2}\right)\{\lambda\boldsymbol{I}+\boldsymbol{F}(\lambda\pi)\}\left\{\frac{A_2}{B_2}\right\}
\end{aligned}$$

The above equation can be further expressed as

$$\begin{aligned}
&\Gamma\left\{\kappa_1\boldsymbol{I}-\lambda\boldsymbol{H}\left(\frac{\pi}{2}\right)\boldsymbol{F}\left(\frac{\lambda\pi}{2}\right)+\lambda\boldsymbol{F}\left(\frac{\lambda\pi}{2}\right)\boldsymbol{H}\left(-\frac{\pi}{2}\right)\right.\\
&\left.+\boldsymbol{F}\left(\frac{\lambda\pi}{2}\right)\boldsymbol{F}\left(\frac{\lambda\pi}{2}\right)\right\}\left\{\frac{A_1}{B_1}\right\}\\
&=\left\{\begin{array}{l}\Gamma\lambda\boldsymbol{F}\left(\frac{\lambda\pi}{2}\right)\boldsymbol{H}\left(-\frac{\pi}{2}\right)-\Gamma\lambda\boldsymbol{F}\left(\frac{\lambda\pi}{2}\right)+\Gamma\boldsymbol{I}-\Gamma\boldsymbol{F}\left(\frac{\lambda\pi}{2}\right)\boldsymbol{F}(\lambda\pi)\\ +\kappa_2\boldsymbol{I}-\lambda\boldsymbol{H}\left(\frac{\pi}{2}\right)\boldsymbol{F}\left(\frac{\lambda\pi}{2}\right)+\lambda\boldsymbol{F}\left(\frac{\lambda\pi}{2}\right)+\boldsymbol{F}\left(\frac{\lambda\pi}{2}\right)\boldsymbol{F}(\lambda\pi)\end{array}\right\}\left\{\frac{A_2}{B_2}\right\}
\end{aligned}\tag{A.13}$$

By virtue of the relationship between $\boldsymbol{H}(\xi)$ and $\boldsymbol{F}(\xi)$, Eq. (A.13) can be reduced to

$$\begin{aligned}
&\Gamma(\kappa_1+1)\left\{\frac{A_1}{B_1}\right\}=\left\{(\kappa_2+\Gamma)\right.\\
&\left.\boldsymbol{I}-(1-\Gamma)\boldsymbol{F}\left(\frac{\lambda\pi}{2}\right)\left[\lambda\left(\boldsymbol{I}-\boldsymbol{H}\left(-\frac{\pi}{2}\right)\right)+\boldsymbol{F}(\lambda\pi)\right]\right\}\left\{\frac{A_2}{B_2}\right\}
\end{aligned}\tag{A.14}$$

By substituting Eqs. (A.7) and (A.12) into Eq. (A.10), the following equation can be obtained:

$$\begin{aligned}
&\left\{\lambda\boldsymbol{I}+\boldsymbol{H}\left(-\frac{\pi}{2}\right)\boldsymbol{H}(\lambda\pi)\boldsymbol{F}\left(\frac{\lambda\pi}{2}\right)\right\}\\
&\left\{\frac{A_1}{B_1}\right\}-\boldsymbol{H}\left(-\frac{\pi}{2}\right)\left\{\lambda\boldsymbol{H}\left(-\frac{\pi}{2}\right)+\boldsymbol{F}\left(\frac{\lambda\pi}{2}\right)\right\}\left\{\frac{A_1}{B_1}\right\}\\
&+\boldsymbol{H}\left(-\frac{\pi}{2}\right)\left\{\lambda\left(\boldsymbol{H}\left(-\frac{\pi}{2}\right)-\boldsymbol{I}\right)+\boldsymbol{F}\left(\frac{\lambda\pi}{2}\right)-\boldsymbol{F}(\lambda\pi)\right\}\left\{\frac{A_2}{B_2}\right\}\\
&=\left\{\lambda\boldsymbol{I}+\boldsymbol{H}\left(-\frac{\pi}{2}\right)\boldsymbol{H}(\lambda\pi)\boldsymbol{F}\left(\frac{\lambda\pi}{2}\right)\right\}\left\{\frac{A_3}{B_3}\right\}
\end{aligned}$$

Then, the above equation becomes

$$\begin{aligned}
&\left\{\lambda\boldsymbol{I}+\boldsymbol{H}\left(-\frac{\pi}{2}\right)\boldsymbol{H}(\lambda\pi)\boldsymbol{F}\left(\frac{\lambda\pi}{2}\right)-\lambda\boldsymbol{I}-\boldsymbol{H}\left(-\frac{\pi}{2}\right)\boldsymbol{F}\left(\frac{\lambda\pi}{2}\right)\right\}\left\{\frac{A_1}{B_1}\right\}\\
&=-\boldsymbol{H}\left(-\frac{\pi}{2}\right)\left\{\lambda\left(\boldsymbol{H}\left(-\frac{\pi}{2}\right)-\boldsymbol{I}\right)+\boldsymbol{F}\left(\frac{\lambda\pi}{2}\right)-\boldsymbol{F}(\lambda\pi)\right\}\left\{\frac{A_2}{B_2}\right\}\\
&+\left\{\lambda\boldsymbol{I}+\boldsymbol{H}\left(-\frac{\pi}{2}\right)\boldsymbol{H}(\lambda\pi)\boldsymbol{F}\left(\frac{\lambda\pi}{2}\right)-\lambda\boldsymbol{H}\left(-\frac{\pi}{2}\right)-\boldsymbol{H}\left(-\frac{\pi}{2}\right)\boldsymbol{F}(-\lambda\pi)\right\}\left\{\frac{A_3}{B_3}\right\}
\end{aligned}\tag{A.15}$$

Let's multiply both sides of Eq. (A.15) by $\boldsymbol{H}(-\frac{\pi}{2})$

$$\begin{aligned}
&\boldsymbol{F}\left(\frac{\lambda\pi}{2}\right)(\boldsymbol{I}-\boldsymbol{H}(-\lambda\pi))\left\{\frac{A_1}{B_1}\right\}\\
&=\left\{\lambda\left(\boldsymbol{H}\left(-\frac{\pi}{2}\right)-\boldsymbol{I}\right)+\boldsymbol{F}\left(\frac{\lambda\pi}{2}\right)-\boldsymbol{F}(\lambda\pi)\right\}\left\{\frac{A_2}{B_2}\right\}\\
&-\left\{\lambda\left(\boldsymbol{H}\left(-\frac{\pi}{2}\right)-\boldsymbol{I}\right)+\boldsymbol{H}(\lambda\pi)\boldsymbol{F}\left(\frac{\lambda\pi}{2}\right)-\boldsymbol{F}(-\lambda\pi)\right\}\left\{\frac{A_3}{B_3}\right\}
\end{aligned}\tag{A.16}$$

By substituting Eqs. (A.7) and (A.12) into Eq. (A.11), the following equation can be obtained

$$\begin{aligned}
&\Gamma\left\{\kappa_1\boldsymbol{I}-\lambda\boldsymbol{H}\left(\frac{\pi}{2}\right)\boldsymbol{H}(\lambda\pi)\boldsymbol{F}\left(\frac{\lambda\pi}{2}\right)\right\}\left\{\frac{A_1}{B_1}\right\}\\
&+\Gamma\boldsymbol{H}(\lambda\pi)\boldsymbol{F}\left(\frac{\lambda\pi}{2}\right)\left\{\lambda\boldsymbol{H}\left(-\frac{\pi}{2}\right)+\boldsymbol{F}\left(\frac{\lambda\pi}{2}\right)\right\}\left\{\frac{A_1}{B_1}\right\}\\
&-\Gamma\boldsymbol{H}(\lambda\pi)\boldsymbol{F}\left(\frac{\lambda\pi}{2}\right)\left\{\lambda\left(\boldsymbol{H}\left(-\frac{\pi}{2}\right)-\boldsymbol{I}\right)+\boldsymbol{F}\left(\frac{\lambda\pi}{2}\right)-\boldsymbol{F}(\lambda\pi)\right\}\left\{\frac{A_2}{B_2}\right\}\\
&=\left\{\kappa_2\boldsymbol{I}-\lambda\boldsymbol{H}\left(\frac{\pi}{2}\right)\boldsymbol{H}(\lambda\pi)\boldsymbol{F}\left(\frac{\lambda\pi}{2}\right)\right\}\left\{\frac{A_3}{B_3}\right\}\\
&+\boldsymbol{H}(\lambda\pi)\boldsymbol{F}\left(\frac{\lambda\pi}{2}\right)\{\lambda\boldsymbol{I}+\boldsymbol{F}(-\lambda\pi)\}\left\{\frac{A_3}{B_3}\right\}
\end{aligned}$$

Substitute Eq. (A.16) into the above equations to eliminate $\left\{\frac{A_2}{B_2}\right\}$

$$\begin{aligned}
&\Gamma(\kappa_1+1)\left\{\frac{A_1}{B_1}\right\}=\left\{(\kappa_2+\Gamma)\boldsymbol{I}\right.\\
&\left.+(1-\Gamma)\boldsymbol{H}(\lambda\pi)\boldsymbol{F}\left(\frac{\lambda\pi}{2}\right)\begin{bmatrix}\lambda\left(\boldsymbol{I}-\boldsymbol{H}\left(-\frac{\pi}{2}\right)\right)\\ +\boldsymbol{F}(-\lambda\pi)\end{bmatrix}\right\}\left\{\frac{A_3}{B_3}\right\}
\end{aligned}\tag{A.17}$$

Using the Dundurs' parameters (Eq. (8)), Eq. (A.14) can be rewritten as

$$\begin{aligned}
&\left\{\frac{A_1}{B_1}\right\}\\
&=\left\{\frac{1+\beta}{1-\alpha}\boldsymbol{I}+\frac{\alpha-\beta}{1-\alpha}\boldsymbol{F}\left(\frac{\lambda\pi}{2}\right)\left[\lambda\left(\boldsymbol{I}-\boldsymbol{H}\left(-\frac{\pi}{2}\right)\right)+\boldsymbol{F}(\lambda\pi)\right]\right\}\left\{\frac{A_2}{B_2}\right\}
\end{aligned}\tag{A.18}$$

Similarly, Eq. (A.17) can be rewritten as

$$\begin{aligned}
\left\{\frac{A_1}{B_1}\right\}&=\left\{\frac{1+\beta}{1-\alpha}\boldsymbol{I}+\frac{\alpha-\beta}{1-\alpha}\boldsymbol{H}(\lambda\pi)\boldsymbol{F}\left(\frac{\lambda\pi}{2}\right)\left[\lambda\left(\boldsymbol{I}-\boldsymbol{H}\left(-\frac{\pi}{2}\right)\right)\right.\right.\\
&\left.\left.+\boldsymbol{F}(-\lambda\pi)\right]\right\}\left\{\frac{A_3}{B_3}\right\}
\end{aligned}\tag{A.19}$$

From Eq. (A.18), we have

$$\begin{Bmatrix} A_1 \\ B_1 \end{Bmatrix} = \frac{1+\beta}{1-\alpha}\begin{Bmatrix} A_2 \\ B_2 \end{Bmatrix} + \frac{\alpha-\beta}{1-\alpha}\boldsymbol{F}\left(\frac{\lambda\pi}{2}\right)\left[\lambda\left(\boldsymbol{I}-\boldsymbol{H}\left(-\frac{\pi}{2}\right)\right)+\boldsymbol{F}(\lambda\pi)\right]\begin{Bmatrix} A_2 \\ B_2 \end{Bmatrix} \tag{A.20}$$

Eq. (A.20) is multiplied by $\frac{1-\alpha}{\alpha-\beta}\boldsymbol{F}(\frac{\lambda\pi}{2})$ on both sides of the equal sign

$$\frac{1-\alpha}{\alpha-\beta}\boldsymbol{F}\left(\frac{\lambda\pi}{2}\right)\begin{Bmatrix} A_1 \\ B_1 \end{Bmatrix} = \frac{1+\beta}{\alpha-\beta}\boldsymbol{F}\left(\frac{\lambda\pi}{2}\right)\begin{Bmatrix} A_2 \\ B_2 \end{Bmatrix} + \left[\lambda\left(\boldsymbol{I}-\boldsymbol{H}\left(-\frac{\pi}{2}\right)\right)+\boldsymbol{F}(\lambda\pi)\right]\begin{Bmatrix} A_2 \\ B_2 \end{Bmatrix} \tag{A.21}$$

From Eq. (A.21), we can get

$$\begin{Bmatrix} A_1 \\ B_1 \end{Bmatrix} = \frac{1+\beta}{1-\alpha}\begin{Bmatrix} A_3 \\ B_3 \end{Bmatrix} + \frac{\alpha-\beta}{1-\alpha}\boldsymbol{H}(\lambda\pi)\boldsymbol{F}\left(\frac{\lambda\pi}{2}\right)\left[\lambda\left(\boldsymbol{I}-\boldsymbol{H}\left(-\frac{\pi}{2}\right)\right)+\boldsymbol{F}(-\lambda\pi)\right]\begin{Bmatrix} A_3 \\ B_3 \end{Bmatrix} \tag{A.22}$$

$\frac{1-\alpha}{\alpha-\beta}\boldsymbol{H}(\lambda\pi)\boldsymbol{F}(\frac{\lambda\pi}{2})$ multiplies Eq. (A.22)

$$\begin{bmatrix} \lambda\left(\boldsymbol{H}\left(-\frac{\pi}{2}\right)-\boldsymbol{I}\right)-\boldsymbol{F}(-\lambda\pi) \\ +\boldsymbol{H}(\lambda\pi)\boldsymbol{F}\left(\frac{\lambda\pi}{2}\right) \end{bmatrix}\begin{Bmatrix} A_3 \\ B_3 \end{Bmatrix} = \boldsymbol{H}(\lambda\pi)\boldsymbol{F}\left(\frac{\lambda\pi}{2}\right)\left\{-\frac{1-\alpha}{\alpha-\beta}\begin{Bmatrix} A_1 \\ B_1 \end{Bmatrix} + \frac{1+\alpha}{\alpha-\beta}\begin{Bmatrix} A_3 \\ B_3 \end{Bmatrix}\right\} \tag{A.23}$$

Substituting Eqs. (A.21) and (A.23) into Eq. (A.16) gives

$$\begin{aligned} &\boldsymbol{F}\left(\frac{\lambda\pi}{2}\right)(\boldsymbol{I}-\boldsymbol{H}(-\lambda\pi))\begin{Bmatrix} A_1 \\ B_1 \end{Bmatrix} \\ &= -\frac{1-\alpha}{\alpha-\beta}\boldsymbol{F}\left(\frac{\lambda\pi}{2}\right)\begin{Bmatrix} A_1 \\ B_1 \end{Bmatrix} + \frac{1+\alpha}{\alpha-\beta}\boldsymbol{F}\left(\frac{\lambda\pi}{2}\right)\begin{Bmatrix} A_2 \\ B_2 \end{Bmatrix} \\ &-\boldsymbol{H}(\lambda\pi)\boldsymbol{F}\left(\frac{\lambda\pi}{2}\right)\left\{-\frac{1-\alpha}{\alpha-\beta}\begin{Bmatrix} A_1 \\ B_1 \end{Bmatrix} + \frac{1+\alpha}{\alpha-\beta}\begin{Bmatrix} A_3 \\ B_3 \end{Bmatrix}\right\} \end{aligned} \tag{A.24}$$

If Eq. (A.24) is multiplied by $\boldsymbol{F}(\frac{\lambda\pi}{2})$, we have

$$\frac{1-\beta}{1+\alpha}(\boldsymbol{I}-\boldsymbol{H}(-\lambda\pi))\begin{Bmatrix} A_1 \\ B_1 \end{Bmatrix} = \begin{Bmatrix} A_2 \\ B_2 \end{Bmatrix} - \boldsymbol{H}(-\lambda\pi)\begin{Bmatrix} A_3 \\ B_3 \end{Bmatrix} \tag{A.25}$$

Then, we substitute Eq. (A.18) into Eq. (A.25) and multiply the results by $\boldsymbol{H}(\lambda\pi)$

$$\left[\frac{1-\beta}{1+\alpha}(\boldsymbol{I}-\boldsymbol{H}(\lambda\pi))\left\{\begin{matrix} \frac{1+\beta}{1-\alpha}\boldsymbol{I}+\frac{\alpha-\beta}{1-\alpha}\boldsymbol{F}\left(\frac{\lambda\pi}{2}\right) \\ \times\left[\lambda\left(\boldsymbol{I}-\boldsymbol{H}\left(-\frac{\pi}{2}\right)\right)+\boldsymbol{F}(\lambda\pi)\right] \end{matrix}\right\}+\boldsymbol{H}(\lambda\pi)\right] \times\begin{Bmatrix} A_2 \\ B_2 \end{Bmatrix} = \begin{Bmatrix} A_3 \\ B_3 \end{Bmatrix} \tag{A.26}$$

Eq. (A.19) is substituted into Eq. (A.26)

$$\left[\frac{1-\beta}{1+\alpha}(\boldsymbol{I}-\boldsymbol{H}(-\lambda\pi))\left\{\begin{matrix} \frac{1+\beta}{1-\alpha}\boldsymbol{I}+\frac{\alpha-\beta}{1-\alpha}\boldsymbol{H}(\lambda\pi)\boldsymbol{F}\left(\frac{\lambda\pi}{2}\right) \\ \times\left[\lambda\left(\boldsymbol{I}-\boldsymbol{H}\left(-\frac{\pi}{2}\right)\right)+\boldsymbol{F}(-\lambda\pi)\right] \end{matrix}\right\}+\boldsymbol{H}(-\lambda\pi)\right]\begin{Bmatrix} A_3 \\ B_3 \end{Bmatrix} = \begin{Bmatrix} A_2 \\ B_2 \end{Bmatrix} \tag{A.27}$$

Eq. (A.1) can be further substituted into Eq. (A.26),

$$\left[\frac{1-\beta}{1+\alpha}\begin{pmatrix} 1-e^{2i\lambda\pi} & 0 \\ 0 & 1-e^{-2i\lambda\pi} \end{pmatrix}\left\{\begin{matrix} \frac{1+\beta}{1-\alpha}\begin{pmatrix} 1 & 0 \\ 0 & 1 \end{pmatrix}+\frac{\alpha-\beta}{1-\alpha}\begin{pmatrix} 0 & e^{-i\lambda\pi} \\ e^{i\lambda\pi} & 0 \end{pmatrix} \\ \times\left[\begin{matrix} \lambda\begin{pmatrix} 1-e^{-i\pi} & 0 \\ 0 & 1-e^{i\pi} \end{pmatrix} \\ +\begin{pmatrix} 0 & e^{-2i\lambda\pi} \\ e^{2i\lambda\pi} & 0 \end{pmatrix} \end{matrix}\right] \end{matrix}\right\}+\begin{pmatrix} e^{2i\lambda\pi} & 0 \\ 0 & e^{-2i\lambda\pi} \end{pmatrix}\right] \times\begin{Bmatrix} A_2 \\ B_2 \end{Bmatrix} = \begin{Bmatrix} A_3 \\ B_3 \end{Bmatrix}$$

The above equation can be simplified to a form,

$$\begin{pmatrix} \chi_1 & \chi_2 \\ \chi_2 & \chi_1 \end{pmatrix}\begin{Bmatrix} A_2 \\ B_2 \end{Bmatrix} = \begin{Bmatrix} A_3 \\ B_3 \end{Bmatrix} \tag{A.28}$$

with

$$\chi_1 = \frac{1-\beta}{1+\alpha}\left(\frac{1+\beta}{1-\alpha}+\frac{\alpha-\beta}{1-\alpha}e^{i\lambda\pi}\right)\left(1-e^{2i\lambda\pi}\right)+e^{2i\lambda\pi}$$

$$\chi_2 = -\frac{1-\beta}{1+\alpha}\frac{\alpha-\beta}{1-\alpha}\lambda\left(1-e^{i\pi}\right)\left(e^{i\lambda\pi}-e^{-i\lambda\pi}\right)$$

Similarly, we substitute Eq. (A.1) into Eq. (A.27) and obtainwhich can be reduced to

$$\begin{pmatrix} \eta_1 & \eta_2 \\ \eta_2 & \eta_1 \end{pmatrix}\begin{Bmatrix} A_3 \\ B_3 \end{Bmatrix} = \begin{Bmatrix} A_2 \\ B_2 \end{Bmatrix} \tag{A.29}$$

with

$$\eta_1 = \frac{1-\beta}{1+\alpha}\left(\frac{1+\beta}{1-\alpha}+\frac{\alpha-\beta}{1-\alpha}e^{-i\lambda\pi}\right)\left(1-e^{-2i\lambda\pi}\right)+e^{-2i\lambda\pi}$$

$$\eta_2 = \frac{1-\beta}{1+\alpha}\frac{\alpha-\beta}{1-\alpha}\lambda\left(1-e^{i\pi}\right)\left(e^{i\lambda\pi}-e^{-i\lambda\pi}\right)$$

Finally, Eq. (A.29) is substituted into Eq. (A.28)which can be rewritten as

$$\begin{pmatrix} \rho_1 & \rho_2 \\ \overline{\rho_2} & \overline{\rho_1} \end{pmatrix} \begin{Bmatrix} A_3 \\ \overline{B_3} \end{Bmatrix} = 0 \tag{A.30}$$

with

$$\rho_1 = \chi_1\eta_1 + \chi_2\overline{\eta_2} - 1$$
$$= 2\left(\alpha+\beta^2\right) - 4\lambda^2\left(\alpha-\beta-\alpha\beta+\beta^2\right) + \left(1-\beta^2\right)\left(e^{-i\lambda\pi}+e^{i\lambda\pi}\right)$$

$$\rho_2 = \chi_1\eta_2 + \chi_2\overline{\eta_1} = \left[\frac{1-\beta}{1+\alpha}\left(\frac{1+\beta}{1-\alpha}+\frac{\alpha-\beta}{1-\alpha}e^{i\lambda\pi}\right)\right.$$
$$\left(1-e^{2i\lambda\pi}\right)+e^{2i\lambda\pi}\left]\left[\frac{1-\beta}{1+\alpha}\frac{\alpha-\beta}{1-\alpha}\lambda\left(1-e^{i\pi}\right)\left(e^{i\lambda\pi}-e^{-i\lambda\pi}\right)\right]\right.$$
$$-\left[\frac{1-\beta}{1+\alpha}\frac{\alpha-\beta}{1-\alpha}\lambda\left(1-e^{i\lambda\pi}\right)\left(e^{i\lambda\pi}-e^{-i\lambda\pi}\right)\right]\left[\frac{1-\beta}{1+\alpha}\left(\frac{1+\beta}{1-\alpha}\right.\right.$$
$$\left.\left.+\frac{\alpha-\beta}{1-\alpha}e^{i\lambda\pi}\right)\left(1-e^{2i\lambda\pi}\right)+e^{2i\lambda\pi}\right] = 0$$

Thus, Eq. (A.30) becomes

$$\begin{pmatrix} \rho_1 & 0 \\ 0 & \overline{\rho_1} \end{pmatrix} \begin{Bmatrix} A_3 \\ \overline{B_3} \end{Bmatrix} = 0 \tag{A.31}$$

According to the theory of linear algebra, the condition that the undetermined coefficient in the Goursat's stress function has a non-zero solution is that the coefficient determinant in Eq. (A.31) equals zero, namely,

$$\left[2\left(\alpha+\beta^2\right) - 4\lambda^2\left(\alpha-\beta-\alpha\beta+\beta^2\right) + \left(1-\beta^2\right)\left(e^{-i\lambda\pi}+e^{i\lambda\pi}\right)\right]$$
$$\times\left[2\left(\alpha+\beta^2\right) - 4\lambda^2\left(\alpha-\beta-\alpha\beta+\beta^2\right) + \left(1-\beta^2\right)\left(e^{i\lambda\pi}+e^{-i\lambda\pi}\right)\right] = 0 \tag{A.32}$$

After simplification, Eq. (A.9) can be further expressed as

$$\frac{\alpha+\beta^2+\left(1-\beta^2\right)\cos\lambda\pi}{2\lambda^2} = (\alpha-\beta)(1-\beta) \tag{A.33}$$

Appendix B. Deriving induced stress on stratigraphic interface

In order to determine the specific expression of the stress field at the HF tip, it is necessary to know the undetermined coefficients (A_j, B_j, C_j, and D_j) in Goursat's stress function. Now let $A = A_1 + B_1$, then, other coefficients can be expressed by A. Combining Eqs. (6a), (6b) and (6e), we can eliminate C_j and D_j and obtain

$$\begin{Bmatrix} A_1 \\ \overline{B_1} \end{Bmatrix} = \begin{pmatrix} \frac{1+\beta}{1-\alpha}+\frac{\alpha-\beta}{1-\alpha}e^{i\lambda\pi} & \frac{\alpha-\beta}{1-\alpha}\lambda e^{-i\lambda\pi}\left(1-e^{i\pi}\right) \\ \frac{\alpha-\beta}{1-\alpha}\lambda e^{i\lambda\pi}\left(1-e^{-i\pi}\right) & \frac{1+\beta}{1-\alpha}+\frac{\alpha-\beta}{1-\alpha}e^{-i\lambda\pi} \end{pmatrix} \times \begin{Bmatrix} A_2 \\ \overline{B_2} \end{Bmatrix} \tag{B.1}$$

After simplification, Eq. (B.1) transforms

$$\begin{cases} A_1 = \left(\frac{1+\beta}{1-\alpha}+\frac{\alpha-\beta}{1-\alpha}e^{i\lambda\pi}\right)A_2 + \left[\frac{\alpha-\beta}{1-\alpha}\lambda e^{-i\lambda\pi}\left(1-e^{i\pi}\right)\right]\overline{B_2} \\ \overline{A_1} = \left(\frac{1+\beta}{1-\alpha}+\frac{\alpha-\beta}{1-\alpha}e^{-i\lambda\pi}\right)\overline{A_2} + \left[\frac{\alpha-\beta}{1-\alpha}\lambda e^{i\lambda\pi}\left(1-e^{-i\pi}\right)\right]B_2 \\ B_1 = \left[\frac{\alpha-\beta}{1-\alpha}\lambda e^{-i\lambda\pi}\left(1-e^{i\pi}\right)\right]\overline{A_2} + \left(\frac{1+\beta}{1-\alpha}+\frac{\alpha-\beta}{1-\alpha}e^{i\lambda\pi}\right)B_2 \\ \overline{B_1} = \left[\frac{\alpha-\beta}{1-\alpha}\lambda e^{i\lambda\pi}\left(1-e^{-i\pi}\right)\right]A_2 + \left(\frac{1+\beta}{1-\alpha}+\frac{\alpha-\beta}{1-\alpha}e^{-i\lambda\pi}\right)\overline{B_2} \end{cases} \tag{B.2}$$

Then, Eq. (B.2) can be further reduced to

$$\begin{cases} (1-\alpha)(A_1+B_1) = \left(1+\beta+(\alpha-\beta)e^{i\lambda\pi}\right)(A_2+B_2) + \left[2(\alpha-\beta)\lambda e^{-i\lambda\pi}\right](\overline{A_2}+\overline{B_2}) \\ (1-\alpha)(\overline{A_1}+\overline{B_1}) = \left(1+\beta+(\alpha-\beta)e^{-i\lambda\pi}\right)(\overline{A_2}+\overline{B_2}) + \left[2(\alpha-\beta)\lambda e^{i\lambda\pi}\right](A_2+B_2) \end{cases} \tag{B.3}$$

By substitution of the first expression of Eq. (B.3) into its second equation, we obtain

$$(1-\alpha)\overline{A} - \frac{1+\beta+(\alpha-\beta)e^{-i\lambda\pi}}{2(\alpha-\beta)\lambda e^{-i\lambda\pi}}(1-\alpha)A$$
$$= \left\{2(\alpha-\beta)\lambda e^{i\lambda\pi} - \frac{\left[1+\beta+(\alpha-\beta)e^{-i\lambda\pi}\right]\left[1+\beta+(\alpha-\beta)e^{i\lambda\pi}\right]}{2(\alpha-\beta)\lambda e^{-i\lambda\pi}}\right\}$$
$$\times(A_2+B_2) \tag{B.4}$$

Subsequently, Eq. (B.4) is simplified to be

$$(A_2+B_2) = \frac{1-\alpha}{\Delta_1}\left[\left(1+\beta+(\alpha-\beta)e^{-i\lambda\pi}\right)A - \left(2(\alpha-\beta)\lambda e^{-i\lambda\pi}\right)\overline{A}\right] \tag{B.5}$$

where $\Delta_1 = (1+\beta)^2 + (1-4\lambda^2)(\alpha-\beta)^2 + 2(1+\beta)(\alpha-\beta)\cos\lambda\pi$.

Similarly, we used A_1+B_1 to replace C_1+D_1 by combining Eqs. (6a) and (6e)

$$C_1+D_1 = \lambda(A_1+B_1) - e^{-i\lambda\pi}(\overline{A_1}+\overline{B_1}) - 2\lambda(A_2+B_2)$$
$$+\left(e^{-i\lambda\pi}-e^{-2i\lambda\pi}\right)(\overline{A_2}+\overline{B_2})$$
$$= \lambda A - e^{-i\lambda\pi}\overline{A} - 2\lambda(A_2+B_2) + \left(e^{-i\lambda\pi}-e^{-2i\lambda\pi}\right)(\overline{A_2}+\overline{B_2})$$
$$= bA + c\overline{A} \tag{B.6}$$

with

$$b=\lambda\left(1-\frac{2(1-\alpha^2)}{\Delta_1}\right) \tag{B.7}$$

$$c=-e^{-i\lambda\pi}+\frac{1-\alpha}{\Delta_1}\left[(1+\beta)e^{-i\lambda\pi}\left(1-e^{-i\lambda\pi}\right)+(\alpha-\beta)\left(1+\left(4\lambda^2-1\right)e^{-i\lambda\pi}\right)\right] \tag{B.8}$$

Combining Eq. (4) and (B.6), we have

$$\sigma_{\theta 1}+i\tau_{r\theta 1}=r^{\lambda-1}\left[A\lambda^2e^{i(\lambda-1)\theta}+\overline{A}\lambda e^{-i(\lambda-1)\theta}+(bA+c\overline{A})\lambda e^{i(\lambda+1)\theta}\right] \tag{B.9}$$

The stress intensity factor is defined by the stress ahead of the HF tip (not on the interface), as given by

$$(\sigma_{\theta 1}+i\tau_{r\theta 1})_{\theta=0}=r^{\lambda-1}\left[A\lambda^2+\overline{A}\lambda+\lambda bA+\lambda c\overline{A}\right]=r^{\lambda-1}K \tag{B.10}$$

after simplification,

$$K=K_1+iK_2=A\lambda^2+\overline{A}\lambda+\lambda bA+\lambda c\overline{A} \tag{B.11}$$

where K_1 represents the opening-mode (mode I) stress intensity factor, and K_2 represents the shearing-mode stress intensity factor.

Eq. (B.11) can be rewritten as

$$\overline{K}=\overline{A}\lambda^2+A\lambda+\lambda b\overline{A}+\lambda\overline{c}A \tag{B.12}$$

Combining Eqs. (B.11) and (B.12), we get

$$\overline{A}=\frac{(1+\overline{c})K-(\lambda+b)\overline{K}}{\lambda(1+\overline{c})(1+c)-\lambda(\lambda+b)^2} \tag{B.13}$$

Substituting Eq. (B.13) into the first equation of Eq. (B.9), the stress component on the stratigraphic interface can be derived

$$\sigma_{\theta 1}+i\tau_{r\theta 1}=\frac{r^{\lambda-1}e^{\frac{i(\lambda-1)\pi}{2}}}{(\lambda+b)^2-(1+c)(1+\overline{c})}\times\left\{\begin{array}{l}K\left[\lambda^2-b^2+(1+\overline{c})e^{-i\lambda\pi}+c(1+\overline{c})\right]\\+\overline{K}\left[-(\lambda+b)e^{-i\lambda\pi}-\lambda(1+2c)+b\right]\end{array}\right\} \tag{B.14}$$

References

Abe, A., Kim, T.W., Horne, R.N., 2021. Laboratory hydraulic stimulation experiments to investigate the interaction between newly formed and preexisting fractures. Int. J. Rock Mech. Min. Sci. 141, 104665. https://doi.org/10.1016/j.ijrmms.2021.104665.

Adachi, J.I., 2001. Fluid-driven Fracture in Permeable Rock. PhD Thesis. Minneapolis University of Minnesota.

Akisanya, A.R., Meng, C.S., 2003. Initiation of fracture at the interface corner of bimaterial joints. J. Mech. Phys. Solid. 51 (1), 27–46. https://doi.org/10.1016/S0022-5096(02)00076-5.

AlTammar, M.J., Agrawal, S., Sharma, M.M., 2019. Effect of geological layer properties on hydraulic-fracture initiation and propagation: an experimental study. SPE J. 24 (2), 757–794. https://doi.org/10.2118/184871-PA.

Blanton, T.L., 1986. Propagation of hydraulically and dynamically induced fractures in naturally fractured reservoirs. SPE Unconventional Gas Technology Symposium. https://doi.org/10.2118/15261-ms.

Bogy, D.B., 1968. Edge-bonded dissimilar orthogonal elastic wedges under normal and shear loading. J. Appl. Mech. 35 (3), 460–466. https://doi.org/10.1115/1.3601236.

Cheng, W., Jin, Y., Chen, M., 2015. Experimental study of step-displacement hydraulic fracturing on naturally fractured shale outcrops. J. Geophys. Eng. 12 (4), 714–723. https://doi.org/10.1088/1742-2132/12/4/714.

Ciambella, J., Bezazi, A., Saccomandi, G., Scarpa, F., 2015. Nonlinear elasticity of auxetic open cell foams modeled as continuum solids. J. Appl. Phys. 117, 184902. https://doi.org/10.1063/1.4921101.

Cook, T.S., Erdogan, F., 1972. Stresses in bonded materials with a crack perpendicular to the interface. Int. J. Eng. Sci. 10 (8), 677–697. https://doi.org/10.1016/0020-7225(72)90063-8.

Dahi Taleghani, A., Gonzalez-Chavez, M., Yu, H., Asala, H., 2018. Numerical simulation of hydraulic fracture propagation in naturally fractured formations using the cohesive zone model. J. Pet. Sci. Eng. 165, 42–57. https://doi.org/10.1016/j.petrol.2018.01.063.

Detournay, E., 2004. Propagation regimes of fluid-driven fractures in impermeable rocks. Int. J. GeoMech. 4, 1–11. https://doi.org/10.1061/(asce)1532-3641 (2004) 4:1(35).

Dundurs, J., 1967. Effect of elastic constants on stress in a composite under plane deformation. J. Compos. Mater. 1 (3), 310–322. https://doi.org/10.1177/002199836700100306.

Elices, M., Guinea, G.V., Gómez, J., Planas, J., 2001. The cohesive zone model: advantages, limitations and challenges. Eng. Fract. Mech. 69 (2), 137–163. https://doi.org/10.1016/S0013-7944(01)00083-2.

Fisher, K., Warpinski, N., 2012. Hydraulic-fracture-height growth: real data. SPE Prod. Oper. 27 (1), 8–19. https://doi.org/10.2118/145949-pa.

Flewelling, S.A., Tymchak, M.P., Warpinski, N., 2013. Hydraulic fracture height limits and fault interactions in tight oil and gas formations. Geophys. Res. Lett. 40 (14), 3602–3606. https://doi.org/10.1002/grl.50707.

Fung, R.L., Vijayakumar, S., Cormack, D.E., 1987. Calculation of vertical fracture containment in layered formations. SPE Form. Evaluation 2 (4), 518–522. https://doi.org/10.2118/14707-PA.

Gao, Q., Ghassemi, A., 2020. Three dimensional finite element simulations of hydraulic fracture height growth in layered formations using a coupled hydro-mechanical model. Int. J. Rock Mech. Min. Sci. 125, 104137. https://doi.org/10.1016/j.ijrmms.2019.104137.

Greengard, L., Kropinski, M.C., Mayo, A., 1996. Integral equation methods for Stokes flow and isotropic elasticity in the plane. J. Comput. Phys. 125 (2), 403–414. https://doi.org/10.1006/jcph.1996.0102.

Gu, H., Siebrits, E., 2008. Effect of formation modulus contrast on hydraulic fracture height containment. SPE Prod. Oper. 1–9. https://doi.org/10.2118/103822-pa.

Gu, H., Weng, X., Lund, J., MacK, M., Ganguly, U., Suarez-Rivera, R., 2012. Hydraulic fracture crossing natural fracture at nonorthogonal angles: a criterion and its validation. SPE Prod. Oper. 27 (1), 20–26. https://doi.org/10.2118/139984-PA.

Guo, J., Luo, B., Lu, C., Lai, J., Ren, J., 2017. Numerical investigation of hydraulic fracture propagation in a layered reservoir using the cohesive zone method. Eng. Fract. Mech. 186, 195–207. https://doi.org/10.1016/j.engfracmech.2017.10.013.

Ham, S.M., Kwon, T.H., 2020. Photoelastic observation of toughness-dominant hydraulic fracture propagation across an orthogonal discontinuity in soft, viscoelastic layered formations. Int. J. Rock Mech. Min. Sci. 134, 104438. https://doi.org/10.1016/j.ijrmms.2020.104438.

Jabbari, N., Aminzadeh, F., de Barros, F.P.J., 2017. Hydraulic fracturing and the environment: risk assessment for groundwater contamination from well casing failure. Stoch. Environ. Res. Risk Assess. 31, 1527–1542. https://doi.org/10.1007/s00477-016-1280-0.

Jiang, Y., Lian, H., Nguyen, V.P., Liang, W., 2019. Propagation behavior of hydraulic fracture across the coal-rock interface under different interfacial friction coefficients and a new prediction model. J. Nat. Gas Sci. Eng. 68, 102894. https://doi.org/10.1016/j.jngse.2019.05.007.

Keller, J., Maus, I., Schlottig, G., Pape, H., Wunderle, B., Michel, B., 2010. Interface fracture mechanics evaluation by correlation of experiment and simulation. Electronics System Integration Technology Conference. https://doi.org/10.1109/ESTC.2010.5642934.

Khoramishad, H., Crocombe, A.D., Katnam, K.B., Ashcroft, I.A., 2010. Predicting fatigue damage in adhesively bonded joints using a cohesive zone model. Int. J. Fatig. 32 (7), 1146–1158. https://doi.org/10.1016/j.ijfatigue.2009.12.013.

Labudovic, V., 1984. Effect of Poisson's ratio on fracture height. JPT, J. Pet. Technol. 21 (6), 1–15. https://doi.org/10.2118/10307-PA.

Lecampion, B., Bunger, A., Zhang, X., 2018. Numerical methods for hydraulic fracture propagation: a review of recent trends. J. Nat. Gas Sci. Eng. 49, 66–83. https://doi.org/10.1016/j.jngse.2017.10.012.

Lei, Z., Yang, X., Li, X., Hu, D., Wu, Y., Peng, Y., 2019. Advanced modeling of horizontal well performance under different re-fracturing designs in tight oil reservoir. SPE Europec Featured at 81st EAGE Conference and Exhibition. https://doi.org/10.2118/195483-ms.

Liu, W., Yao, J., Zeng, Q., 2021. A numerical hybrid model for non-planar hydraulic fracture propagation in ductile formations. J. Pet. Sci. Eng. 196, 107796. https://doi.org/10.1016/j.petrol.2020.107796.

Llanos, E.M., Jeffrey, R.G., Hillis, R., Zhang, X., 2017. Hydraulic fracture propagation through an orthogonal discontinuity: a laboratory, analytical and numerical study. Rock Mech. Rock Eng. 50, 2101–2118. https://doi.org/10.1007/s00603-017-1213-3.

Lu, C., Li, M., Guo, J.C., Tang, X.H., Zhu, H.Y., Yong-Hui, W., Liang, H., 2015. Engineering geological characteristics and the hydraulic fracture propagation mechanism of the sand-shale interbedded formation in the Xu5 reservoir. J. Geophys. Eng. 12 (3), 321–339. https://doi.org/10.1088/1742-2132/12/3/321.

Ming-Yuan, H., Hutchinson, J.W., 1989. Crack deflection at an interface between dissimilar elastic materials. Int. J. Solid Struct. 25 (9), 1053–1067. https://doi.org/10.1016/0020-7683(89)90021-8.

Park, K., Paulino, G.H., 2011. Cohesive zone models: a critical review of traction-separation relationships across fracture surfaces. Appl. Mech. Rev. 64 (6),

060802. https://doi.org/10.1115/1.4023110.
Peng, B., Li, Q., Feng, X.Q., Gao, H., 2021. Effect of shear stress on adhesive contact with a generalized Maugis-Dugdale cohesive zone model. J. Mech. Phys. Solid. 148, 104275. https://doi.org/10.1016/j.jmps.2020.104275.
Renshaw, C.E., Pollard, D.D., 1995. An experimentally verified criterion for propagation across unbounded frictional interfaces in brittle, linear elastic materials. Int. J. Rock Mech. Min. Sci. 32 (3), 237–249. https://doi.org/10.1016/0148-9062(94)00037-4.
Rodriguez, J., Heo, J., Kim, K.H., 2020. The impact of hydraulic fracturing on groundwater quality in the permian Basin, West Texas, USA. Water 12 (3), 796. https://doi.org/10.3390/w12030796.
Simonson, E.R., Abou-Sayed, A.S., Clifton, R.J., 1978. Containment of massive hydraulic fractures. SPE J. 18 (1), 27–32. https://doi.org/10.2118/6089-pa.
Smith, M.B., Bale, A.B., Britt, L.K., Klein, H.H., Siebrits, E., Dang, X., 2001. Layered modulus effects on fracture propagation, proppant placement, and fracture modeling. SPE Annual Technical Conference and Exhibition. https://doi.org/10.2118/71654-ms.
Tan, P., Jin, Y., Han, K., Zheng, X., Hou, B., Gao, J., Chen, M., Zhang, Y., 2017. Vertical propagation behavior of hydraulic fractures in coal measure strata based on true triaxial experiment. J. Pet. Sci. Eng. 158, 398–407. https://doi.org/10.1016/j.petrol.2017.08.076.
Tan, P., Jin, Y., Yuan, L., Xiong, Z.Y., Hou, B., Chen, M., Wan, L.M., 2019. Understanding hydraulic fracture propagation behavior in tight sandstone–coal interbedded formations: an experimental investigation. Petrol. Sci. 16, 148–160. https://doi.org/10.1007/s12182-018-0297-z.
Tang, X., Rutqvist, J., Hu, M., Rayudu, N.M., 2019. Modeling Three-dimensional fluid-driven propagation of multiple fractures using TOUGH-FEMM. Rock Mech. Rock Eng. 52, 611–627. https://doi.org/10.1007/s00603-018-1715-7.
Thiercelin, M., Jeffrey, R.G., Naceur, K. Ben, 1989. Influence of fracture toughness on the geometry of hydraulic fractures. SPE Prod. Eng. 4 (4), 435–442. https://doi.org/10.2118/16431-pa.
van Eekelen, H.A.M., 1982. Hydraulic fracture geometry: fracture containment in layered formations. Soc. Petrol. Eng. J. https://doi.org/10.2118/9261-PA.
Wang, H., Liu, H., Wu, H.A., Wang, X.X., 2015. A 3D numerical model for studying the effect of interface shear failure on hydraulic fracture height containment. J. Pet. Sci. Eng. 133, 280–284. https://doi.org/10.1016/j.petrol.2015.06.016.
Warpinski, N.R., 2011. Hydraulic fracture height in gas shale reservoirs. SEG Tech. Progr. Expand. Abstr. https://doi.org/10.1190/1.3627971.
Warpinski, N.R., Schmidt, R.A., Northrop, D.A., 1982. In-situ stresses: the predominant influence on hydraulic fracture containment. J. Petrol. Technol. 34 (3), 653–664. https://doi.org/10.2118/8932-PA.
Weng, X., Chuprakov, D., Kresse, O., Prioul, R., Wang, H., 2018. Hydraulic fracture-height containment by permeable weak bedding interfaces. Geophysics 83 (3), 137–152. https://doi.org/10.1190/GEO2017-0048.1.
Wolhart, S.L., Stutz, H.L., Mayerhofer, M.J., 2004. Applying advanced fracture diagnostics to optimize fracture stimulation in coalbed methane reservoirs: case history of two fields in the Rocky Mountains. SPE Eastern Regional Meeting. https://doi.org/10.2118/91376-MS.
Wu, T., Fang, H., Sun, H., Zhang, F., Wang, X., Wang, Y., Li, S., 2021. A data-driven approach to evaluate fracturing practice in tight sandstone in Changqing field. International Petroleum Technology Conference. https://doi.org/10.2523/iptc-21821-MS.
Xing, P., Yoshioka, K., Adachi, J., El-Fayoumi, A., Bunger, A.P., 2018. Laboratory demonstration of hydraulic fracture height growth across weak discontinuities. Geophysics 83 (2), 93–105. https://doi.org/10.1190/geo2016-0713.1.
Yin, Z., Huang, H., Zhang, F., Zhang, L., Maxwell, S., 2020. Three-dimensional distinct element modeling of fault reactivation and induced seismicity due to hydraulic fracturing injection and backflow. J. Rock Mech. Geotech. Eng. 12 (4), 752–767. https://doi.org/10.1016/j.jrmge.2019.12.009.
Yue, K., Lee, H.P., Olson, J.E., Schultz, R.A., 2020. Apparent fracture toughness for LEFM applications in hydraulic fracture modeling. Eng. Fract. Mech. 230, 106984. https://doi.org/10.1016/j.engfracmech.2020.106984.
Zhang, F., Dontsov, E., Mack, M., 2017a. Fully coupled simulation of a hydraulic fracture interacting with natural fractures with a hybrid discrete-continuum method. Int. J. Numer. Anal. Methods GeoMech. 41 (13), 1430–1452. https://doi.org/10.1002/nag.2682.
Zhang, F., Zhu, H., Zhou, H., Guo, J., Huang, B., 2017b. Discrete-element-method/computational-fluid-dynamics coupling simulation of proppant embedment and fracture conductivity after hydraulic fracturing. SPE J. 22, 632–644. https://doi.org/10.2118/185172-PA.
Zhang, F., Damjanac, B., Maxwell, S., 2019. Investigating hydraulic fracturing complexity in naturally fractured rock masses using fully coupled multiscale numerical modeling. Rock Mech. Rock Eng. 52, 5137–5160. https://doi.org/10.1007/s00603-019-01851-3.
Zhang, F., Yin, Z., Chen, Z., Maxwell, S., Zhang, L., Wu, Y., 2020a. Fault reactivation and induced seismicity during multistage hydraulic fracturing: microseismic analysis and geomechanical modeling. SPE J. 25 (2), 692–711. https://doi.org/10.2118/199883-PA.
Zhang, X., Jeffrey, R.G., 2008. Reinitiation or termination of fluid-driven fractures at frictional bedding interfaces. J. Geophys. Res. Solid Earth 113, B08416. https://doi.org/10.1029/2007JB005327.
Zhang, Y., Zhao, Y., Yang, H., Wang, C., 2020b. A semianalytical solution for a Griffith crack nonuniformly pressurized by internal fluid. Rock Mech. Rock Eng. 53, 2439–2460. https://doi.org/10.1007/s00603-020-02052-z.
Zhao, D., Chen, Z., Cai, X., et al., 2007. Analysis of distribution rule of geostress in China. Chin. J. Rock Mech. Eng. 185 (6), 1265–1271. https://doi.org/10.3321/j.issn:1000-6915.2007.06.024 (**in Chinese**).
Zhao, H., Ma, F., Liu, G., Feng, X., Guo, J., 2018. Analytical investigation of hydraulic fracture-induced seismicity and fault activation. Environ. Earth Sci. 77, 526. https://doi.org/10.1007/s12665-018-7708-8.
Zhao, Y., He, P., Zhang, Y., Wang, C., 2019. A new criterion for a toughness-dominated hydraulic fracture crossing a natural frictional interface. Rock Mech. Rock Eng. 52, 2617–2629. https://doi.org/10.1007/s00603-018-1683-y.
Zhao, Y., Wang, C.L., Bi, J., 2020. Analysis of fractured rock permeability evolution under unloading conditions by the model of elastoplastic contact between rough surfaces. Rock Mech. Rock Eng. 53 (53), 5795–5808. https://doi.org/10.1007/s00603-020-02224-x.
Zhao, Y., Bi, J., Wang, C., Liu, P., 2021a. Effect of unloading rate on the mechanical behavior and fracture characteristics of sandstones under complex triaxial stress conditions. Rock Mech. Rock Eng. 54, 4851–4866. https://doi.org/10.1007/s00603-021-02515-x.
Zhao, Y., Wang, C., Teng, M., Bi, J., 2021b. Observation on microstructure and shear behavior of mortar due to thermal shock. Cem. Concr. Compos. 121, 104106. https://doi.org/10.1016/j.cemconcomp.2021.104106.
Zhao, Y., Wang, C., Ning, L., Zhao, H., Bi, J., 2022a. Pore and fracture development in coal under stress conditions based on nuclear magnetic resonance and fractal theory. Fuel 309, 122112. https://doi.org/10.1016/j.fuel.2021.122112.
Zhao, Y., Zhang, Y., Yang, H., Liu, Q., Tian, G., 2022b. Experimental study on relationship between fracture propagation and pumping parameters under constant pressure injection conditions. Fuel 307, 121789. https://doi.org/10.1016/j.fuel.2021.121789.
Zhou, J., Chen, M., Jin, Y., Zhang, G. qing, 2008. Analysis of fracture propagation behavior and fracture geometry using a tri-axial fracturing system in naturally fractured reservoirs. Int. J. Rock Mech. Min. Sci. 45 (7), 1143–1152. https://doi.org/10.1016/j.ijrmms.2008.01.001.
Zhuang, X., Zhou, S., Sheng, M., Li, G., 2020. On the hydraulic fracturing in naturally-layered porous media using the phase field method. Eng. Geol. 266, 105306. https://doi.org/10.1016/j.enggeo.2019.105306.
Zou, Y.S., Ma, X.F., Zhou, T., Li, N., et al., 2017. Hydraulic fracture growth in a layered formation based on fracturing experiments and discrete element modeling. Rock Mech. Rock Eng. 50, 2381–2395. https://doi.org/10.1007/s00603-017-1241-z.